

Age and metallicity gradients in early-type galaxies: a dwarf-to-giant sequence

Mina Koleva,^{1,2,3,*} Philippe Prugniel,³ Sven De Rijcke⁴ and Werner W. Zeilinger⁵

¹*Instituto de Astrofísica de Canarias, La Laguna, E-38200 Tenerife, Spain*

²*Departamento de Astrofísica, Universidad de La Laguna, E-38205 La Laguna, Tenerife, Spain*

³*Université Lyon 1, Villeurbanne F-69622, France; CRAL, Observatoire de Lyon, St Genis Laval F-69561, France; CNRS, UMR 5574*

⁴*Department of Physics and Astronomy, Ghent University, Krijgslaan 281, S9, B-9000 Ghent, Belgium*

⁵*Institut für Astronomie, Universität Wien, Türkenschanzstrasse 17, A-1180 Wien, Austria*

Accepted 2011 May 11. Received 2011 May 10; in original form 2010 December 9

ABSTRACT

We studied the stellar populations of 40 early-type galaxies using medium-resolution long-slit spectroscopy along their major axes (and along the minor axis for two of them). The sample, including elliptical and lenticular galaxies as well as dwarf galaxies, is combined with other previously published data in order to discuss the systematics of the radial gradients of age and metallicity over a large mass range, from $10^7 M_{\odot}$ to $10^{12} M_{\odot}$ ($-9.2 > M_B > -22.4$ mag). The well-known mass–metallicity relation is continuous throughout the whole mass range, in the sense that more massive galaxies are more metal-rich. The age–mass relation is consistent with the idea of downsizing: smaller galaxies have more extended star formation histories than more massive ones. The transition-type dwarfs (intermediate between dwarf irregular and dwarf elliptical galaxies) deviate from this relation having younger mean age, and the low-mass dwarf spheroidals have older ages, marking a discontinuity in the relation, possibly due to selection effects.

In all mass regimes, the mean metallicity gradients are approximately -0.2 and the mean age gradients $+0.1$ dex per decade of radius. The individual gradients are widely spread: $-0.1 < \nabla_{\text{Age}} < 0.4$ and $-0.54 < \nabla_{[\text{Fe}/\text{H}]} < +0.2$. We do not find evidence for a correlation between the metallicity gradient and luminosity, velocity dispersion, central age or age gradient. Likewise, we do not find a correlation between the age gradient and any other parameter in bright early-type galaxies. In faint early-types with $M_B \gtrsim -17$ mag, on the other hand, we find a strong correlation between the age gradient and luminosity: the age gradient becomes more positive for fainter galaxies. Together with the observed downsizing phenomenon this indicates that, as time passes, star formation persists in dwarf galaxies and becomes more centrally concentrated. However, this prolonged central star formation is not reflected in the metallicity profiles of the dwarfs in our sample.

We conclude that various physical mechanisms can lead to similar gradients and that these gradients are robust against the environmental effects. In particular, the gradients observed in dwarf galaxies certainly survived the transformation of the progenitors through tidal harassment or/and ram-pressure stripping. The diversity of metallicity gradients amongst dwarf elliptical galaxies may reflect a plurality of progenitors' morphologies. The dwarfs with steep metallicity gradients could have originated from blue compact dwarfs and those with flat profiles from dwarf irregulars and late-type spirals.

Key words: galaxies: dwarf – galaxies: elliptical and lenticular, cD – galaxies: evolution – galaxies: formation – galaxies: kinematics and dynamics – galaxies: stellar content.

*E-mail: koleva@iac.es

1 INTRODUCTION

The internal inhomogeneities of galaxies offer a valuable insight into their chemical and dynamical evolution, and their star formation histories. The radial age and metallicity gradients in a galaxy are the result of its star formation and metal enrichment history. The stellar population may have originated from pristine gas and continued forming from self-enriched gas flowing to the galaxy centre, creating negative gradients in the mean metallicity and positive gradients in the mean age (Larson 1974; Pipino, D’Ercole & Matteucci 2008). To persist and be observed, the gradients must survive the galaxy’s evolution. The ageing of the stellar population erases the observational signatures of age gradients and fades the mean metallicity gradients. Orbital mixing and merger events will also alter them (White 1980; Kobayashi 2004; Di Matteo et al. 2009). Thus, the gradients are likely related to other properties of the galaxies and should reflect the diversity of the formation and evolution processes. We can a priori expect the mass to play the first role, and we may expect different trends in different mass regimes, in fact reflecting different formation mechanisms.

The monolithic collapse models of Pipino et al. (2010) predict gradients in the range $-0.5 < \Delta[\text{Fe}/\text{H}]/\Delta\log(r) \equiv \nabla_{[\text{Fe}/\text{H}]} < -0.2$ dex per decade of radius (computed within the effective radius, r_{eff}). Those gradients appear to be independent of the galaxies’ masses (their fig. 4). The dispersion results from initial conditions and reflects the competition between feedback and star formation. As an alternative mechanism, smoothed-particle hydrodynamic (SPH) simulations (Bekki & Shioya 1999; Hopkins et al. 2009) suggest that the dispersion of the metallicity gradients (between -0.6 and 0) is due to the diversity of (wet) mergers. Mergers may destroy the gradients but can also induce star formation to regenerate them. These gradients do not depend on the progenitor’s mass.

A hybrid formation scenario, involving collapse, merging histories (Kormendy 1989; Ogando et al. 2005) and ram-pressure quenching of the star formation (for the smallest galaxies) may possibly account for the diversity of histories and characteristics of early-type galaxies.

Gradients of age and metallicity have been observed in normal elliptical and S0 galaxies ($M > 10^{10} M_{\odot}$). They are determined comparing spectra or colours to models of single stellar populations (SSPs). These SSP-equivalent parameters are dominated by the most luminous stars and hence by the youngest star formation event. They are closer to luminosity-weighted than to mass-weighted characteristics, but still they should not be confused with the former. Colour gradients were observed in E galaxies back in the 1960s (e.g. de Vaucouleurs 1961) and were generally interpreted as metallicity gradients. Similar conclusions were reached by studying the radial distribution of spectral line strengths (McClure 1969; Carollo, Danziger & Buson 1993). In the recent years, more elaborated approaches were used to simultaneously determine the age and the metallicity. Sánchez-Blázquez et al. (2007) conclude that the line-strength gradients are essentially due to metallicity and that the age of the populations is generally homogeneous. Analogous results are also reached in Mehlert et al. (2003) and Rawle, Smith & Lucey (2010): the metallicity gradients are spread around $\nabla_{[\text{Fe}/\text{H}]} \approx -0.2$ ($-0.5 < \nabla_{[\text{Fe}/\text{H}]} < 0.2$). Sánchez-Blázquez, Gorgas & Cardiel (2006a) find no, or at most a marginal, correlation between the metallicity gradients and the mass of the galaxies or their large-scale environment. However, Forbes, Sánchez-Blázquez & Proctor (2005) support a correlation between the metallicity gradient and

the mass in the sense that more massive galaxies have steeper negative gradients. Annibali et al. (2007) studied intermediate and massive early-type galaxies ($120 \text{ km s}^{-1} < \sigma_{\text{central}} < 300 \text{ km s}^{-1}$) and find negative metallicity gradients (-0.2), which decrease with the increase of the mass.

Until recently, less information was available concerning the low-mass, early-type galaxies ($M_B > -18$ mag; $L < 10^9 L_{\odot}$). Most of them are dwarf, diffuse elliptical (dE) galaxies, with smooth elliptical isophotes, exponential surface brightness profiles and in general quiescent. They are predominantly observed in galaxy clusters or as satellites of massive galaxies. They differ from ‘normal’ ellipticals (E) by their lower concentration (Kormendy 1985; Kormendy et al. 2009), although a small population of objects intermediate between dEs and Es exists (e.g. Prugniel 1994).

Some recent studies present evidence for a diversity of age and metallicity gradients in dEs (Chilingarian 2009; Koleva et al. 2009a). On average, negative metallicity gradients, $\nabla_{[\text{Fe}/\text{H}]} = -0.26$, and positive age gradients, $\Delta\log(\text{Age})/\Delta\log(r) \equiv \nabla_{\text{Age}} = +0.1$, were found, but with large dispersions. They are in the range $-0.5 < \nabla_{[\text{Fe}/\text{H}]} < 0.4$ and $-0.1 < \nabla_{\text{Age}} < 0.3$. About 1/3 of the galaxies have flat profiles that may be connected with rotation or with the presence of a disc (Koleva et al. 2009a), but otherwise, no significant correlation with any galaxy property was found.

Descending through the mass sequence of the early-type galaxies ($M \leq 10^{8-9} M_{\odot}$), a diversity of gradients was found. Makarova et al. (2010) found no gradient in two dwarf spheroidals (dSphs) of the M81 group, KDG 61 and 64 ($M_B \approx -13$ mag). Lianou, Grebel & Koch (2010) confirmed the homogeneity of these two galaxies, but found negative photometric metallicity gradients ($\nabla_{[\text{Fe}/\text{H}]} \approx -0.1 \sim -0.2$ within r_{eff}) in two other dwarfs of this group, out of the eight they studied. In Centaurus A group dE/dSph ($-10 < M_B < -14$), Crnojević, Grebel & Koch (2010) detected weak metallicity gradients, typically of the order of $\nabla_{[\text{Fe}/\text{H}]} \sim -0.07$.

Harbeck et al. (2001) searched for population gradients at even lower masses ($M < 10^8$) in nine Local Group dSphs through horizontal-branch morphologies and distributions of red giant branch and red clump stars. Negative metallicity gradients are suggested in Sextans, Sculptor, Tucana and Andromeda VI, and possibly a positive age gradient in the Carina dSph. No population gradient is found in Andromeda I, II, III and V. Positive age gradients were found in the Fornax (Stetson, Hesser & Smecker-Hane 1998) and Sextans (Okamoto et al. 2008) dSphs and in the transition-type galaxy Phoenix (Martínez-Delgado, Gallart & Aparicio 1999). Further spectroscopic studies of individual stars confirmed the metallicity gradient in Sextans (Kleyna et al. 2004; Battaglia et al. 2011) and Sculptor (Tolstoy et al. 2004; Kirby et al. 2009) and revealed gradients in Fornax (Battaglia et al. 2006) and probably in Leo I (Gullieuszik et al. 2009). A negative metallicity gradient is also detected in the disrupted Sagittarius dwarf (Keller, Yong & Da Costa 2010). A general feature is that whenever population gradients are found in dSphs, they are negative in metallicity and positive in age. In the three galaxies with a large number of spectroscopic measurements, Fornax, Sculptor and Sextans, the metallicity gradients are $\nabla_{[\text{Fe}/\text{H}]} \approx -0.3$.

The star-forming Sm and dIrr galaxies may be the progenitors of the quiescent dwarfs. However, the metallicity of their interstellar medium, estimated from H II regions, appears homogeneous (Kobulnicky & Skillman 1997; van Zee, Skillman & Haynes 2006), but the metallicity of their old stellar populations is generally not constrained by the present observations. The stellar population of the Large Magellanic Cloud (LMC) shows only a shallow negative

metallicity gradient, and the Small Magellanic Cloud (SMC) seems to be chemically homogeneous (Cioni 2009; Feast, Abedigamba & Whitelock 2010).

All these studies suggest that the metallicity gradients in early-type galaxies are spread around a negative value, without any strong correlation with the mass of the system. However, a recent study by Spolaor et al. (2009), including one dE/dS0, presents a tight relation between the metallicity gradient and the central velocity dispersion or mass, leading from strong gradients in normal E/S0 to flat profiles in dEs.

In this paper, we address questions related to stellar population gradients in medium- to low-mass early-type galaxies. Our aim is to describe the systematics of the gradients in early-type systems. We will study various samples of low-mass galaxies, including those of Koleva et al. (2009a) and Spolaor et al. (2009). We analyse with the same method data from different instruments and compare the results obtained by different authors and using different approaches.

The paper is organized as follows. In Section 2, we introduce the samples and describe the data processing. In Section 3 we analyse the data and derive the gradients, and in Section 4 we will compare our results with previous studies. In Section 5 we present discussions, and Section 6 draws conclusions.

2 OBSERVATIONS AND DATA REDUCTION

To investigate the systematics of the population gradients in low-mass, early-type galaxies, we gathered a sample of galaxies with good quality spectroscopic data available in the telescope archives. The main sample was presented in De Rijcke et al. (2005) and was focused on dE galaxies. We also included the sample of Spolaor et al. (2009). To verify the robustness of the analysis, we used the observations of S0 galaxies used in Bedregal et al. (2006) and those of E galaxies presented in Vazdekis et al. (2001, hereafter VAKU), containing several objects in common with the previous samples. Finally, we include NGC 205 (Simien & Prugniel 2002) and NGC 404 (Bouchard et al. 2010), which are two nearby galaxies that have been studied in detail.

For all these galaxies, we use spectroscopic long-slit data acquired along the major axis, and for NGC 205 and 404 along the minor axis too. To refine the morphological classification of the galaxies we use photometric studies from the literature (the corresponding references can be found in Table 1 and Appendix C). For the Spolaor et al. sample, we gathered images and did our proper analyses (see Appendix A).

Although all the galaxies can be broadly qualified as ‘early-type’, the full sample contains a mix of morphologies. We re-examined these objects and separated them in four groups: (1) ‘normal’ elliptical galaxies ($M_B < -18$ mag), (2) S0 ($M_B < -18$ mag), (3) dE and dS0 and (4) transition-type dwarf (TTD) galaxies. The distinction between the former two classes and the latter two is made on the basis of luminosity and concentration. To separate E and S0 galaxies we examined the isophotes shape, the V_{\max}/σ_0 ratios (where V_{\max} is the maximum projected velocity of rotation and σ_0 the central velocity dispersion) and the signatures of discs or dust lanes on the images. Finally, to distinguish dEs/dS0s from TTD galaxies we considered their star formation histories (a galaxy with constant star formation rate, until present will be classified as a TTD) and the H I or H α detections.

Even if NGC 205 is detected in H I and H α we consider it as a dE/dS0 because its H I is only $5.3 \times 10^5 M_{\odot}$ (Young & Lo 1997), while the detection limit at the distance of Virgo is $3 \times 10^6 M_{\odot}$

(Conselice et al. 2003¹). The spectrum extracted in a 100 pc aperture does not show prominent emission in the Balmer lines (though these emission lines are clearly visible after subtracting the stellar component). We associated the compact elliptical galaxy (cE), NGC 4486B = VCC 1297, to the E group, as cEs are more related to Es than to dEs (Kormendy 1985; Nieto & Prugniel 1987).

The characteristics of the 40 galaxies are presented in Table 1. Below, we give details about the data and processing.

2.1 De Rijcke et al. sample

This sample, of 16 dE/dS0 galaxies, was observed with the FORS1 and FORS2 spectrographs attached to the Very Large Telescope (VLT). These observations were used in De Rijcke et al. (2001, 2003a,b, 2004, 2005), Michielsen et al. (2004, 2007) and Koleva et al. (2009a) to study the kinematics and stellar population of dE galaxies. For the present study, we use the reduced spectroscopic data described in Koleva et al. (2009a).

The FORS1 data have a resolution $\Delta\lambda = 2.6 \text{ \AA}$ and cover the wavelength range 3300–6200 \AA . The FORS2 data have a resolution of $\Delta\lambda = 3.0 \text{ \AA}$ and cover the wavelength range 4355–5640 \AA . All the data have central signal-to-noise ratio (S/N) values of typically 30 per wavelength element.

To analyse the data, and in particular the kinematics, the instrumental broadening of the observations with respect to the model needs to be accurately determined. This is characterized by the line-spread function (LSF) and depends on the wavelength. The LSF is determined from twilight and stellar template spectra using the full spectrum fitting package ULYSS (Koleva et al. 2009b). It compares observations to models having a finite resolution. Thus, it measures the excess of broadening of the former with respect to the latter; this is why we speak of the *relative* LSF.

We adopted LSFs with mean broadening of $\sigma_{\text{LSF}} = 63$ and 73 km s^{-1} for the FORS1 and FORS2 observations, respectively. Note that due to the relatively wide slit of 1 arcsec, the FORS2 have a lower spectral resolution and the centres of the galaxies are marginally spatially resolved within the slit (i.e. the total broadening is the combination of the intrinsic resolution of the spectrograph, the width of the slit, the spatial profile and the internal kinematics of the galaxies). Since the luminosity profiles are known, it is in principle possible to take them into account and recover reliable kinematics. However, we do not focus on the galaxies’ dynamics and we will not attempt these complicated corrections. For these reasons, the velocity dispersion profiles must be interpreted with care, as well as the velocities in the central arcsec. The internal kinematics of these galaxies were separately determined using higher resolution observations presented in De Rijcke et al. (2005).

2.2 Spolaor et al. sample

The Spolaor et al. sample consists of 14 galaxies, six in the Fornax cluster (FCC 148, FCC 153, FCC 170, FCC 277, FCC 301 and FCC 335) and eight in the Virgo cluster (VCC 575, VCC 828, VCC 1025, VCC 1146, VCC 1178, VCC 1297, VCC 1475 and VCC 1630). Most of the Fornax cluster galaxies are S0s. Two of them, FCC 153 and FCC 170, are seen edge-on and display a prominent disc component. Another galaxy, VCC 1327 = NGC 4486A,

¹ Note that with a detection limit of $2 \times 10^7 M_{\odot}$ the ALFALFA survey (di Serego Alighieri et al. 2007) is less deep than the observations used in Conselice et al. (2003).

Table 1. Structural properties of our sample. The columns are as follows: name of the galaxy in Virgo and Fornax catalogues, other name, type, apparent magnitude in B , absolute magnitude in B , central velocity dispersion in km s^{-1} , ellipticity, effective radius in arcsec, surface brightness at the effective radius in B , Sérsic index, samples: 1 – De Rijcke et al., 2 – Spolaor et al., 3 – Bedregal et al., 4 – VAKU, 5 – NGC 205, 6 – NGC 404, comments. The measurements are ours, except where indicated. The De Rijcke et al. galaxies' properties are taken from their paper.

F/VCC	Name	Type	M_B^a (mag)	M_B^b (mag)	σ (km s^{-1})	ϵ^c	R_e (arcsec)	$\mu_{e,B}$ (mag arcsec $^{-2}$)	Sérsic d n	s	Comment
E											
FCC 277	NGC 1428	E-S0	13.62	-17.7	82	0.50	13.7	20.55	1.93	2	–
VCC 0575	NGC 4318	E	14.07	-17.6	95	0.32	7.8	20.10	1.66	2	Discy
VCC 0731	NGC 4365	E	10.39	-20.4	256	0.11	35.1	22.11	7.11	4	Boxy, triaxial, KDC
VCC 0828	NGC 4387	E	12.97	-18.3	115	0.41	26.0	20.17	2.33	2,4	Boxy
VCC 1025	NGC 4434	E	12.96	-18.8	120	0.04	10.6	20.05	2.26	2	Elliptical isophotes
VCC 1146	NGC 4458	E	13.07	-18.2	103	0.07	14.8	20.84	2.16	2	Elliptical isophotes, KDC
VCC 1178	NGC 4464	E	13.45	-17.4	129	0.25	6.0	19.55	2.31	2,4	Discy
VCC 1231	NGC 4473	E	10.91	-19.9	179	0.41	12.5	20.39	4.00	4	KDC
VCC 1279	NGC 4478	E	12.16	-19.0	144	0.19	17.0	19.82	2.07	4	–
VCC 1297	NGC 4486B	cE	14.22	-16.8	170	0.03	2.7	18.38	2.63	2	Discy
VCC 1475	NGC 4515	E-S0	13.42	-17.8	86	0.21	10.5	20.27	2.71	2	Discy innerparts
VCC 1630	NGC 4551	E	12.87	-18.3	107	0.26	15.0	20.43	1.78	2	Slightly boxy
VCC 1903	NGC 4621	E	10.52	-20.3	225	0.26	27.7	21.72	5.36	4	KDC
S0											
FCC 021	NGC 1316	S0	9.29	-22.3	226	0.42	46.3	21.61	2.90	3	Dust, merger?
FCC 055	ESO 358-006	S0	13.90	-17.5	47	0.48	5.3	21.50	3.00	3	–
FCC 148	NGC 1375	S0	13.05	-18.2	69	0.56	9.1	20.59	1.69	2,3	Peanut bulge
FCC 153	IC 0335	S0	12.84	-18.5	79	0.69	5.8	20.63	1.83	2,3	Thin edge-on disc
FCC 167	NGC 1380	S0	10.80	-20.8	221	0.51	15.9	20.79	3.30	3	–
FCC 170	NGC 1381	S0	12.02	-19.0	150	0.62	4.3	19.18	3.10	2,3	Big bulge, thin disc
FCC 177	NGC 1380A	S0	13.21	-18.1	67	0.72	8.7	21.92	3.70	3	–
FCC 301	ESO 358-059	E-S0	13.95	-17.4	49	0.17	3.4	20.60	4.36	2,3	–
dE/dS0											
	[FS90]029	dE5	15.70	-17.5	60	0.54	8.9	22.44	1.79	1	–
	[FS90]075	dE1,N	16.87	-16.3	49	0.10	6.8	23.03	1.74	1	–
	[FS90]076	dE1	16.10	-17.1	57	0.07	4.4	21.41	2.02	1	KDC
	[FS90]131	dE5,N	15.30	-17.9	87	0.54	8.1	21.83	2.35	1	Peanut
	NGC 5898 DW1	dE3	15.66	-17.6	44	0.34	8.7	22.35	1.53	1	–
FCC 043	IC1919	dE3	13.91	-17.8	56	0.26	16.9	22.05	2.17	1	–
FCC 136		dE2	14.81	-16.9	64	0.21	14.2	22.57	1.71	1	–
FCC 150		dE4,N	15.70	-16.0	64	0.19	5.7	21.48	1.65	1	–
FCC 204	ESO 358-043	dS0	14.76	-17.0	67	0.61	11.5	22.06	1.29	1	Spiral
FCC 245		dE0,N	16.00	-15.7	40	0.11	11.4	23.28	1.35	1	–
FCC 266		dE0,N	15.90	-15.8	42	0.11	7.1	22.15	1.08	1	–
FCC 288	ESO 358-056	dS0	15.10	-16.6	49	0.72	9.5	21.99	1.11	1	Spiral
FCC 335	ESO 359-002	dS0,N	14.50	-17.1	44	0.34	15.4	21.99	1.55	2,3	–
	NGC 205	dE5	8.61	-16.0	20	0.39	147.9	21.82		5	H I, H α emission
TTD											
	NGC 404	dS0	11.19	-16.5	30	0.00	42.0	21.05	2.43	6	H I, H α emission, LINER
	[FS90]373	dE3	15.60	-17.8	73	0.23	7.9	22.03	2.71	1	KDC
	NGC 5898 DW2	dS0,N	16.10	-17.2	44	0.57	5.9	21.95	1.26	1	H α emission
FCC 046		dE4,N	15.99	-15.7	61	0.36	6.7	22.12	1.24	1	H I, H α emission
FCC 207		dE2,N	16.19	-15.5	61	0.15	8.4	22.81	1.32	1	H α emission

^aValues for sample 4 (without repetitive observations) are taken from HyperLeda.

^bComputed using the following distance modulus: Virgo – 30.8, Fornax – 31.6, NGC 5898 group – 32.6, NGC 5044 – 32.87, NGC 3258 – 33.00, NGC 205 – 24.5, for NGC 404 we adopt a distance of 3.4 Mpc (Tonry et al. 2001). All measurements were corrected for galactic extinction and reddening.

^c $\epsilon = 1 - b/a$, with b/a being the minor-to-major axial ratio of the isophotes. For samples 3, 4, 5, 6 we list values from HyperLeda.

^dValues for sample 4 were taken from Kormendy et al. (2009), and for sample 6 from Seth et al. (2010).

was also observed in the Virgo programme. This low-luminosity E galaxy was set apart from the present sample because its spectra, highly contaminated by the light of a 12th magnitude foreground star, located 2 arcsec from the nucleus, deserved a special treatment. Its kinematical and population analysis is presented in Prugniel et al.

(2011). The surface photometry obtained from the image taken in the GMOS archive is presented in Appendix A.

The GMOS long-slit spectra of the Fornax and Virgo sample were extracted from the *Gemini* data archive. The Virgo and Fornax data sets have the same characteristics with the exception of the

spectral resolution as a result of different slit widths (0.5 and 1.0 arcsec, respectively). The details of the two setups are given in Table 2, while the log of the observations is in Table 3. At least two spectra were obtained for each target galaxy. All the spectra were observed by aligning the slit with the optical

Table 2. Setup of observations.

GMOS @ Gemini South – Fornax cluster	
CCDs, EEV number	2037-06-03/8194-19-04/8261-07-04
No. of pixels	3 × 2048 × 4068 chips
Pixel size (μm^2)	13.5 × 13.5
Image scale (arcsec pixel $^{-1}$)	0.0727
Readout noise (e $^{-}$ pixel $^{-1}$)	3.98/3.85/3.16
Gain [ADU (e $^{-}$) $^{-1}$]	2.372/2.076/2.097
Grism	B600_G5323
Slit width (arcsec)	1.0
Spectral range (Å)	3690–6450
FWHM $\delta\lambda$ (Å)	4.7
σ_{instr} (km s $^{-1}$)	114
Dispersion (Å pixel $^{-1}$)	0.46
GMOS @ Gemini South – Virgo cluster	
CCDs, EEV number	2037-06-03/8194-19-04/8261-07-04
No. of pixels	3 × 2048 × 4068 chips
Pixel size (μm^2)	13.5 × 13.5
Image scale (arcsec pixel $^{-1}$)	0.0727
Readout noise (e $^{-}$ pixel $^{-1}$)	3.20/3.50/3.10
Gain [ADU (e $^{-}$) $^{-1}$]	2.000/1.900/1.900
Grism	B600_G5323
Slit width (arcsec)	0.5
Spectral range (Å)	3640–6500
FWHM $\delta\lambda$ (Å)	2.5
σ_{instr} (km s $^{-1}$)	61
Dispersion (Å pixel $^{-1}$)	0.46
FORS2 @ VLT – Fornax cluster	
CCDs, MIT/LL mosaic number	CCID20-14-5-3
No. of pixels	2 × 4096 × 2068 chips
Pixel size (μm^2)	15
Image scale (arcsec pixel $^{-1}$)	0.126
Readout noise (e $^{-}$ pixel $^{-1}$)	2.7/3.60
Gain [ADU (e $^{-}$) $^{-1}$]	0.8/0.8
Grism	GRIS_1400V
Slit width (arcsec)	0.51
Spectral range (Å)	4560–5900
FWHM $\delta\lambda$ (Å)	1.1
σ_{instr} (km s $^{-1}$)	19.9
Dispersion (Å pixel $^{-1}$)	0.32
ISIS @ 4.2 WHT – VAKU sample	
No. of pixels	3471–5501
Image scale (arcsec pixel $^{-1}$)	0.439
Slit width (arcsec)	1.6
Spectral range (Å)	3978–5501
FWHM $\Delta\lambda$ (Å)	2.4
σ_{instr} (km s $^{-1}$)	58.8
CARELEC @ 1.93 OHP – NGC 205 and 404	
No. of pixels	2048
Image scale (arcsec pixel $^{-1}$)	0.54
Slit width (arcsec)	1.5
Spectral range (Å)	4700–5600
FWHM $\Delta\lambda$ (Å)	1.4
σ_{instr} (km s $^{-1}$)	35

Table 3. Observation log.

Instrument	Object	λ_0 (Å)	Exposure (s)	Slit PA
GMOS-S (Fornax)	FCC 148	5075	4 × 2040.5	90
	FCC 153	5075	4 × 2040.5	83
	FCC 170	5075	3 × 2040.5	139
	FCC 277	5075	4 × 2040.5	116
		5075	4 × 2040.5	122
	FCC 301	5075	4 × 2040.5	155
	FCC 335	5075	2 × 2040.5	47
GMOS-S (Virgo)	VCC 0575	5250	2 × 1886.5	65
		5300	2 × 1886.5	65
	VCC 0828	5250	2 × 1886.5	3
		5300	2 × 1886.5	3
	VCC 1025	5250	3 × 1886.5	15
		5300	2 × 1886.5	15
	VCC 1146	5250	2 × 1886.5	174
		5300	2 × 1886.5	174
	VCC 1178	5250	2 × 1886.5	10
		5300	2 × 1886.5	10
	VCC 1297	5250	2 × 1886.5	100
		5300	2 × 1886.5	100
	VCC 1327	5250	2 × 1886.5	18
		5250	1 × 1500.5	18
		5300	4 × 1200.5	18
	VCC 1475	5250	2 × 1886.5	15
		5300	2 × 1886.5	15
	VCC 1630	5200	2 × 1886.5	58
		5300	2 × 1886.5	58
FORS2	FCC 021	5200	3 × 1200	50
	FCC 055	5200	2 × 2400	32
	FCC 148	5200	2 × 1800	90
	FCC 153	5200	2 × 1600	83
	FCC 167	5200	2 × 1200	3
	FCC 170	5200	2 × 1600	42
	FCC 177	5200	2 × 1700	4
	FCC 301	5200	1 × 2550	24
	FCC 335	5200	1 × 2250	47

major axis of the galaxy. The long-slit spectra cover the full extent of the three detectors including two small gaps. In order to cover these gaps additional spectra with a shift of the central wavelength by 50 Å were obtained in the case of FCC 277 and the whole Virgo sample. Since the S/N of the individual data sets was found to be sufficient for the present investigation, we preferred to keep the data sets separate instead of stacking them. We used the second, slightly shifted data set for an independent analysis in order to check the reproducibility of the results.

The data reduction was performed using the IRAF-based GMOS standard pipeline software for bias and flat-field correction and wavelength calibration. Cosmic rays were identified and corrected by the IRAF task CRBLASTER. A sky spectrum was derived for each galaxy spectrum from regions in the spectral image empty of objects. The sky spectrum was then subtracted from the object spectrum.

In the case of the Fornax data, the Gaussian width of the LSF increases from $\sigma_{\text{LSF}} = 100$ to 150 km s $^{-1}$ along the wavelength range. This broadening is larger than the velocity dispersion of most of the target galaxies and a close examination of the night sky emission line profiles reveals that the spectral resolution is determined by the slit profile. Therefore, as for the FORS2 observations described in Section 2.1, the centre of the galaxies is spatially resolved in the slit. Hence, the precision of the velocity dispersion

measurements will be limited. However, except for one galaxy, additional FORS2 spectra (see Section 2.3) can be used to accurately constrain the velocity dispersion. We adopted an average between the LSF derived from the twilight and the template spectra. We checked that the corresponding velocity dispersion agrees with that measured on the FORS2 spectra and found that the velocity dispersion is overestimated in the external regions and, more importantly, it is underestimated in the centres, which produces fake σ -drops (see Appendix C). This problem is not discussed in Spolaor et al. (2010a), where kinematical analyses of these data are also presented. In the case of the Virgo data, the slit width was narrower and the spectral resolution sufficient to derive reliable kinematics. We adopt for the Fornax and Virgo galaxies an LSF of 114 and 61 km s⁻¹, respectively.

2.3 Bedregal et al. sample

The European Southern Observatory (ESO) data archive contains FORS2 long-slit spectra of five of the six Fornax cluster galaxies of the Spolaor et al. sample. An analysis of these data has been published by Bedregal et al. (2006). The spectral resolution of the FORS2 data is higher than the GMOS observations, allowing therefore accurate measurements of the internal stellar kinematics.

The FORS2 setup is described in Table 2. The data reduction was performed using the ESO FORS pipeline software for bias and flat-field correction, distortion correction and wavelength calibration. Cosmic rays were identified and corrected by the IRAF task CRBLASTER. A sky spectrum was derived for each galaxy spectrum from regions in the spectral image empty of objects. The sky spectrum was then subtracted from the object spectrum.

The pipeline data reduction ignored the correction of the electronic noise mentioned by Bedregal et al. (2006). This effect, identified as a 15 Hz hum in the reading of the CCD, produces an aperiodic residual. This artefact may affect the analysis of the stellar population, as it clearly dominates the noise in the external regions. We also analysed the spectra reduced by A. Bedregal including the hum correction, which he courteously made available to us (Koleva et al. 2011). We found a perfect consistency between the two analyses, but a noticeable divergence in the external regions. With the uncorrected data, the metallicity reaches higher values than with the corrected ones. The fact that the corrected version is in a better agreement with the analysis of the GMOS data may be used as an indication of the relevance of the correction. However, in order to keep the analyses independent, we simply chose to limit our analysis to the radial range where the two data sets give consistent results.

We adopt a wavelength-independent Gaussian relative LSF of 19.9 km s⁻¹ determined from template star spectra.

2.4 Vazdekis et al. sample, NGC 205 and 404

The other data sets included in our discussions are from VAKU (six E galaxies from the Virgo cluster), Simien & Prugniel (2002, NGC 205) and Bouchard et al. (2010, NGC 404). The observational setups are presented in Table 2, and their data reduction is described in the corresponding papers. The seeing during these observations was larger than the slit widths; thus we do not expect problems in the derived kinematic profiles.

The reduced Vazdekis et al. data were taken from the HyperLeda² FITS archive, where no associated template star is given. Therefore,

the LSF could not be determined directly, and we derived it in order to match the velocity dispersion profiles of NGC 4387 and 4464 with those obtained from the GMOS data. We checked that the central velocity dispersion of the other four galaxies also agrees with the values compiled in HyperLeda. We used a Gaussian LSF with $\sigma_{\text{LSF}} = 58.8 \text{ km s}^{-1}$, in good agreement with the nominal resolution of 2.4 Å.

For NGC 205 and 404 we used the reduced data and the LSF quoted in the corresponding papers. NGC 205 is a close companion of M31 and a prototype of the dwarf elliptical class of galaxies. NGC 404 is an isolated dwarf S0.

3 ANALYSIS OF THE STELLAR POPULATION AND KINEMATICS

In this section, we first describe the method for extracting the internal kinematics and the SSP-equivalent ages and metallicities. Thereafter, we present the stellar population radial profiles of the 40 galaxies. Then, we measure the population gradients, and finally we discuss possible biases.

3.1 Analysis method

The principle of our analysis is to compare an observed spectrum with a model of a population broadened to account for the internal kinematics. A least-square minimization provides the internal kinematics and the parameters of the population model, age and metallicity in the case of an SSP. This is done with the ULYSS³ package (Koleva et al. 2009b). The main characteristics of the method, described and validated in Koleva et al. (2008b,b), are to fit the full spectrum, pixel-by-pixel, while the most common approach uses spectrophotometric indices. The SSP-equivalent ages and metallicity for central extractions of the De Rijcke et al. sample were found perfectly consistent with Lick indices and three times more precise (Michielsen et al. 2007; Koleva et al. 2011). Besides the precision, another advantage of the method is its insensitivity to the presence of emission lines, that can be either masked or fitted with additional Gaussians.

We are using stellar population models generated with PEGASE-HR⁴ (Le Borgne et al. 2004), assuming Salpeter initial mass function (IMF; Salpeter 1955) and Padova isochrones (Alongi et al. 1993, and companion papers) and build with the ELODIE.3.1 library (Prugniel & Soubiran 2001; Prugniel et al. 2007b). These models have a well-calibrated LSF (i.e. instrumental broadening) of 0.58 Å corresponding to a resolution $R \approx 10000$ or an instrumental velocity dispersion $\sigma_{\text{instr}} = 13 \text{ km s}^{-1}$ at $\lambda = 5500 \text{ Å}$.

The ELODIE library, as any other empirical library, consists mostly of stars of the solar neighbourhood and hence presents the abundance pattern of this environment. Therefore, a model made with such library cannot match a population with non-solar abundances, such as in globular clusters or massive elliptical galaxies known to harbour an excess of Mg with respect to Fe. However, it was found (Koleva et al. 2008a) that the measurements of [Fe/H] and [Mg/Fe] with full-spectrum fitting are independent. In other words, a mismatch of [Mg/Fe] does not affect the measurement of [Fe/H]. For this reason, we preferred to conservatively use the empirical library instead of the α -elements resolved semi-empirical one (Prugniel et al. 2007a) which is not tested in detail.

³ <http://ulyss.univ-lyon1.fr>

⁴ <http://www2.iap.fr/pegase/pegasechr/>

² leda.univ-lyon1.fr (Paturel et al. 2003).

During the fit we perform automatic kappa-sigma clipping to exclude the spikes (un-removed cosmic rays, or artefacts of the subtraction of strong sky lines). The Mg triplet, near 5175 Å, is also masked in the case of strong α -overabundance. The NaD region ($\lambda \sim 589$ nm) is masked by default, since it is strongly affected by the telluric absorption.

The fit is rendered insensitive to the shape of the spectral energy distribution thanks to the inclusion of a multiplicative polynomial in the model. This feature makes the flux-calibration unnecessary. The possible biases due to this polynomial have been well studied on other occasions, and we determined the optimal degree as in Koleva et al. (2009b). The adopted degrees essentially depend of the wavelength range. We used 40 for the GMOS observations, and 25 for all the others.

3.2 Extraction and fit of one-dimensional spectra

For each object, we extract two one-dimensional (1D) spectra integrated within simulated apertures of semimajor axes equal to about 50 pc and $1 a_{\text{eff}}$ where $a_{\text{eff}} = r_{\text{eff}}/\sqrt{1 - \epsilon}$ is the semimajor axis of the effective isophote. The inner extraction is aimed at characterizing the core that may be highly contaminated by a nucleus. To make these extractions, each individual spectrum is weighted by its radius (and consequently the $1 a_{\text{eff}}$ extractions are sometimes noisy).

For the Virgo and Fornax galaxies, the core radius was fixed at 0.5 arcsec, which also corresponds to the seeing disc. The corresponding physical diameters are 106 pc in Fornax and 84 pc in Virgo. For the dEs belonging to more distant groups, we used the same apparent diameter (a smaller extraction would not make sense, because of the seeing limitation). For NGC 205 we adopted a radius of 14 arcsec for the core extraction, and 3 arcsec for NGC 404, to sample a region of about 100 pc of diameter. When computing the outer extractions, we excluded the core region.

The results of the analysis of the core 1D spectra are reported in Table 4. The quality and details of the fits can be checked in Appendix B, where we plot the ones from the central regions (Figs B1–B10).

3.3 Radial profiles

To build the profiles, independent 1D spectra were generated by adding together adjacent observed spectra until $S/N = 40$ was reached. The process was started from the central spectrum and extended successively on both sides. Typically, the central spectrum has $S/N \approx 80$, and therefore the central region is not binned. In the external parts, several spectra are grouped. If the bin width reaches $r_{\text{max}}/r_{\text{min}} = 1.4$, where r_{min} and r_{max} are its inner and outer limits, the target S/N is decreased. The profile is continued until $S/N > 5$. The central spectrum is defined as the peak of wavelength-integrated flux, except for FCC 21 = NGC 1316 which is affected by a strong dust lane. In this case, we used the centre of symmetry of the rotation profile (interestingly, it is not the centre of symmetry of the velocity dispersion profile).

When emission lines were present, $H\beta$, $H\gamma$ and $[\text{O III}]\lambda 5007$ Å, they were fitted with Gaussians together with all the other free parameters.

The error bars, estimated from the noise and quality of the fit, give the independent errors on the age and the metallicity and do not take into account the age–metallicity degeneracy (a metallicity offset is compensated by a bias of the age): some points are deviating from a smooth profile by more than the error bar, but they lie on the same

age–metallicity degeneracy line (or actually age–metallicity– σ surface). The error bars determined from Monte Carlo simulations are about twice larger, as they take also into account the degeneracies.

The radial profiles are shown in Figs 1–5. The corresponding measurements are available in the electronic form at the Centre de Données astronomiques de Strasbourg.⁵ For the De Rijcke et al. sample, the analysis is essentially identical to the one presented in Koleva et al. (2009a), the only difference is that we presently use the official release of ULYSS, while we were previously using a development version (the cleaning algorithm, which rejects the spikes, was improved). The profiles are indiscernible from the published ones, and we do not reproduce them here.

The first point to notice is the high degree of symmetry of the profiles, which is showing that independent, but presumably similar, spectra are leading to consistent results (though this does not tell if those parameters are not biased). When two spectra were analysed, for example for the eight Virgo galaxies observed with GMOS, the two profiles were also in agreement (they are represented with different colours in Fig. 1). Moreover, the profiles derived using different instruments, resolution and wavelength ranges display a remarkable consistency. This can be seen in Figs 2 and 3 where the analysis of the GMOS data is overplotted.

3.4 Population gradients

In this section, we describe the computation of the gradients of the population parameters and present the results.

We fitted the gradients assuming linear relations between $\log \text{Age}$ or $[\text{Fe}/\text{H}]$ and $\log(r/r_{\text{eff}})$:

$$\log \text{Age}(r/r_{\text{eff}}) = \log \text{Age}_{\text{eff}} + \nabla_{\text{Age}} \log(r/r_{\text{eff}}) \quad (1)$$

and

$$[\text{Fe}/\text{H}](r/r_{\text{eff}}) = [\text{Fe}/\text{H}]_{\text{eff}} + \nabla_{[\text{Fe}/\text{H}]} \log(r/r_{\text{eff}}), \quad (2)$$

where ∇_{Age} and $\nabla_{[\text{Fe}/\text{H}]}$ are the fitted population gradients and $\log \text{Age}_{\text{eff}}$ and $[\text{Fe}/\text{H}]_{\text{eff}}$ the fitted age and metallicity at the effective isophote (r/r_{eff} is the galactocentric distance along the considered axis, i.e. along the major axis, it is a/a_{eff}). We used the observed points between a radius of 0.5 arcsec and the effective isophote, weighted with the observational error. The fits of the profiles are presented in Figs 6–9 and the coefficients in Table 4.

As noted by others (e.g. Baes et al. 2007) the profiles are not always well fitted with these power laws. This is reflected by large values of χ^2 . In Table 4, we also list the uncertainty on the metallicity gradient multiplied by χ (i.e. the formal error obtained if the estimated measurement errors are rescaled in order to get $\chi^2 = 1$). This gives an idea of the range of values we would find if we play with the radial limits or if we sample differently the radius of the galaxy.

The mean gradients, for the whole sample of 40 galaxies, and within our four classes, are given in Table 5.

3.5 Verification

The SSP-equivalent parameters are sensitive to the uncertainties in the data reduction and in the population models. This may result not only in random errors, but also in systematics. In Koleva et al. (2009c), we investigated possible sources of error due to the data reduction and, in particular, to the sky subtraction. We concluded

⁵ CDS; <http://vizier.u-strasbg.fr/>

Table 4. Central populations and gradients. E(Age) and E([Fe/H]) are the uncertainties on the gradients rescaled by χ (see Section 3.4).

Name	log Age _{core}	log Age _{eff}	∇_{Age}	E(Age)	[Fe/H] _{core}	[Fe/H] _{eff}	$\nabla_{[\text{Fe}/\text{H}]}$	E([Fe/H])
FCC 277	0.73 ± 0.01	0.89 ± 0.01	0.10 ± 0.01	0.19	-0.07 ± 0.00	-0.50 ± 0.01	-0.33 ± 0.01	0.11
VCC 575	0.80 ± 0.01	1.65 ± 0.03	0.04 ± 0.03	0.20	-0.05 ± 0.01	-0.76 ± 0.03	-0.32 ± 0.02	0.11
VCC 731	1.31 ± 0.00	1.27 ± 0.03	0.08 ± 0.04	0.09	0.01 ± 0.01	-0.14 ± 0.03	-0.14 ± 0.03	0.08
VCC 828	0.96 ± 0.01	1.93 ± 0.03	0.00 ± 0.02	0.14	0.01 ± 0.00	-0.78 ± 0.03	-0.30 ± 0.02	0.11
VCC 1025	0.91 ± 0.01	1.84 ± 0.02	-0.05 ± 0.02	0.09	0.06 ± 0.00	-0.77 ± 0.03	-0.35 ± 0.02	0.07
VCC 1146	0.98 ± 0.00	2.04 ± 0.04	0.05 ± 0.02	0.11	-0.23 ± 0.00	-1.17 ± 0.04	-0.26 ± 0.02	0.08
VCC 1178	1.03 ± 0.00	1.99 ± 0.02	-0.05 ± 0.02	0.10	-0.23 ± 0.00	-0.73 ± 0.03	-0.14 ± 0.02	0.07
VCC 1231	1.01 ± 0.02	1.07 ± 0.02	0.17 ± 0.02	0.15	0.08 ± 0.01	-0.12 ± 0.02	-0.18 ± 0.02	0.10
VCC 1279	0.79 ± 0.01	1.07 ± 0.02	0.24 ± 0.04	0.08	0.11 ± 0.01	-0.31 ± 0.03	-0.35 ± 0.04	0.06
VCC 1297	1.22 ± 0.01	2.28 ± 0.05	-0.10 ± 0.09	0.25	-0.15 ± 0.00	-0.40 ± 0.04	-0.12 ± 0.04	0.09
VCC 1475	0.86 ± 0.01	1.85 ± 0.04	0.06 ± 0.03	0.15	-0.17 ± 0.00	-1.11 ± 0.04	-0.34 ± 0.02	0.14
VCC 1630	0.82 ± 0.00	1.98 ± 0.02	0.12 ± 0.01	0.11	0.15 ± 0.00	-0.54 ± 0.03	-0.30 ± 0.02	0.08
VCC 1903	0.82 ± 0.00	1.11 ± 0.02	0.17 ± 0.02	0.13	0.23 ± 0.01	-0.23 ± 0.02	-0.27 ± 0.02	0.08
FCC 21	0.65 ± 0.03	0.67 ± 0.02	-0.03 ± 0.03	0.14	0.12 ± 0.01	0.07 ± 0.01	-0.00 ± 0.03	0.09
FCC 55	0.61 ± 0.02	0.65 ± 0.03	-0.08 ± 0.07	0.10	-0.25 ± 0.01	-0.34 ± 0.03	-0.03 ± 0.03	0.11
FCC 148	0.15 ± 0.00	0.97 ± 0.01	0.10 ± 0.01	0.12	0.25 ± 0.00	-0.58 ± 0.02	-0.36 ± 0.01	0.10
FCC 153	0.46 ± 0.00	0.57 ± 0.00	-0.00 ± 0.00	0.16	0.26 ± 0.00	0.16 ± 0.00	0.04 ± 0.00	0.09
FCC 167	1.21 ± 0.03	1.11 ± 0.04	-0.09 ± 0.06	0.11	0.07 ± 0.01	-0.21 ± 0.03	-0.22 ± 0.05	0.09
FCC 170	1.04 ± 0.00	0.91 ± 0.00	-0.11 ± 0.01	0.08	-0.09 ± 0.00	-0.13 ± 0.01	-0.01 ± 0.01	0.07
FCC 177	0.29 ± 0.01	0.61 ± 0.02	0.22 ± 0.04	0.18	0.22 ± 0.01	-0.11 ± 0.02	-0.22 ± 0.03	0.09
FCC 301	0.63 ± 0.01	0.72 ± 0.01	0.11 ± 0.01	0.16	-0.14 ± 0.00	-0.29 ± 0.01	-0.17 ± 0.01	0.20
FS029	0.46 ± 0.00	0.48 ± 0.01	-0.09 ± 0.02	0.31	0.04 ± 0.01	-0.28 ± 0.02	-0.19 ± 0.02	0.14
FS075	0.60 ± 0.00	0.67 ± 0.03	0.13 ± 0.05	0.36	0.08 ± 0.00	-0.30 ± 0.03	-0.33 ± 0.03	0.11
FS076	0.79 ± 0.00	0.80 ± 0.03	0.01 ± 0.05	0.44	0.15 ± 0.00	-0.17 ± 0.03	-0.34 ± 0.04	0.19
FS131	0.62 ± 0.01	0.57 ± 0.03	-0.12 ± 0.04	0.40	0.03 ± 0.01	-0.28 ± 0.03	-0.21 ± 0.03	0.16
DW0001	0.54 ± 0.01	0.69 ± 0.01	0.04 ± 0.02	0.23	-0.23 ± 0.00	-0.25 ± 0.02	-0.03 ± 0.02	0.13
FCC 043	0.49 ± 0.01	0.35 ± 0.01	-0.01 ± 0.01	0.21	-0.23 ± 0.01	-0.50 ± 0.01	-0.38 ± 0.02	0.24
FCC 136	0.65 ± 0.01	0.83 ± 0.04	0.16 ± 0.05	0.31	-0.29 ± 0.01	-0.65 ± 0.03	-0.36 ± 0.04	0.25
FCC 150	0.53 ± 0.01	0.62 ± 0.02	0.02 ± 0.04	0.45	-0.38 ± 0.01	-0.70 ± 0.02	-0.39 ± 0.04	0.26
FCC 204	0.35 ± 0.01	0.49 ± 0.01	0.10 ± 0.01	0.23	0.12 ± 0.00	-0.44 ± 0.02	-0.40 ± 0.02	0.19
FCC 245	0.62 ± 0.01	0.61 ± 0.03	0.30 ± 0.05	0.43	-0.64 ± 0.01	-0.59 ± 0.04	-0.08 ± 0.04	0.36
FCC 266	0.60 ± 0.01	0.57 ± 0.02	0.33 ± 0.04	0.57	-0.48 ± 0.01	-0.88 ± 0.03	-0.54 ± 0.04	0.46
FCC 288	0.58 ± 0.01	0.41 ± 0.01	-0.01 ± 0.01	0.28	-0.59 ± 0.01	-0.43 ± 0.01	0.08 ± 0.02	0.23
FCC 335	-0.01 ± 0.01	0.53 ± 0.01	0.30 ± 0.02	0.15	-0.36 ± 0.02	-0.52 ± 0.02	-0.22 ± 0.04	0.19
NGC 205 ma	0.13 ± 0.01	1.02 ± 0.03	0.25 ± 0.01	0.22	-0.59 ± 0.02	-2.04 ± 0.04	-0.29 ± 0.02	0.18
NGC 205 mi	0.11 ± 0.00	0.39 ± 0.02	0.22 ± 0.01	0.23	-0.50 ± 0.01	-0.70 ± 0.02	-0.16 ± 0.03	0.24
NGC 404 ma	0.14 ± 0.01	0.42 ± 0.02	0.18 ± 0.02	0.14	-0.23 ± 0.01	-0.38 ± 0.05	-0.11 ± 0.04	0.12
NGC 404 mi	0.11 ± 0.01	0.33 ± 0.02	0.14 ± 0.02	0.14	-0.18 ± 0.01	-0.25 ± 0.07	-0.05 ± 0.06	0.23
FS373	0.17 ± 0.00	0.50 ± 0.02	0.15 ± 0.02	0.29	0.08 ± 0.00	-0.58 ± 0.03	-0.54 ± 0.03	0.18
DW0002	0.23 ± 0.00	0.37 ± 0.01	0.20 ± 0.01	0.30	-0.92 ± 0.01	-0.37 ± 0.02	0.36 ± 0.03	0.28
FCC 046	0.03 ± 0.00	0.22 ± 0.01	0.22 ± 0.01	0.20	-1.04 ± 0.01	-0.71 ± 0.03	0.21 ± 0.04	0.29
FCC 207	0.10 ± 0.00	0.66 ± 0.02	0.45 ± 0.04	0.52	-0.59 ± 0.02	-0.74 ± 0.03	-0.20 ± 0.04	0.39

that this cannot significantly affect our determination of the gradients. It was also established that the fitted parameters do not depend on S/N, at least down to $S/N \approx 5$ (Koleva et al. 2007, 2009c).

In the present work, we compare the results obtained using our data reduction and the one from Bedregal et al. (2006, 2011), kindly provided to us by the author. We found a bias of the metallicities associated with the (lack of) correction of a defect of the CCD amplifier (see Section 2.3), but this affects only the external regions, generally outwards of $1 r_{\text{eff}}$. Although this would not dramatically impact the determinations of the gradients, we rejected these points.

We tested that our results are independent of the fact that whether we mask or fit (with Gaussians) the emission lines. In all the cases where significant emission lines are seen, we fitted $H\beta$ (and higher order Balmer lines) and $[\text{O III}]\lambda 5007 \text{ \AA}$. We also checked the limitations due to the reliability of the models. We have shown that models using sparsely populated empirical libraries can lead to bias

in the population parameters' recovery (Koleva et al. 2008b), but the rich and large modern libraries considered here are free of such effects. To check the impact of the different physics involved in different stellar population models, we repeated all the analysis with other models. We used the recent models of Vazdekis et al. (2010, version 9) based on the MILES library (Sánchez-Blázquez et al. 2006b), and the unpublished Pegase.HR models also build with MILES. The comparisons between the three sets of models are shown in Figs 10 and 11. All the models give consistent results, though some small trends are visible (see Prugniel et al., in preparation).

Another caveat is hidden in the interpolation in the meshes of the stellar population grid. Often, all the points of a profile are between the same two metallicities of the model grid and sometimes even between the same two age nodes. In case of ULYSS, the interpolation is computed with splines, where the variables are $\log(\text{age})$ and $[\text{Fe}/\text{H}]$. Its accuracy was verified in Koleva et al. (2008b) where the

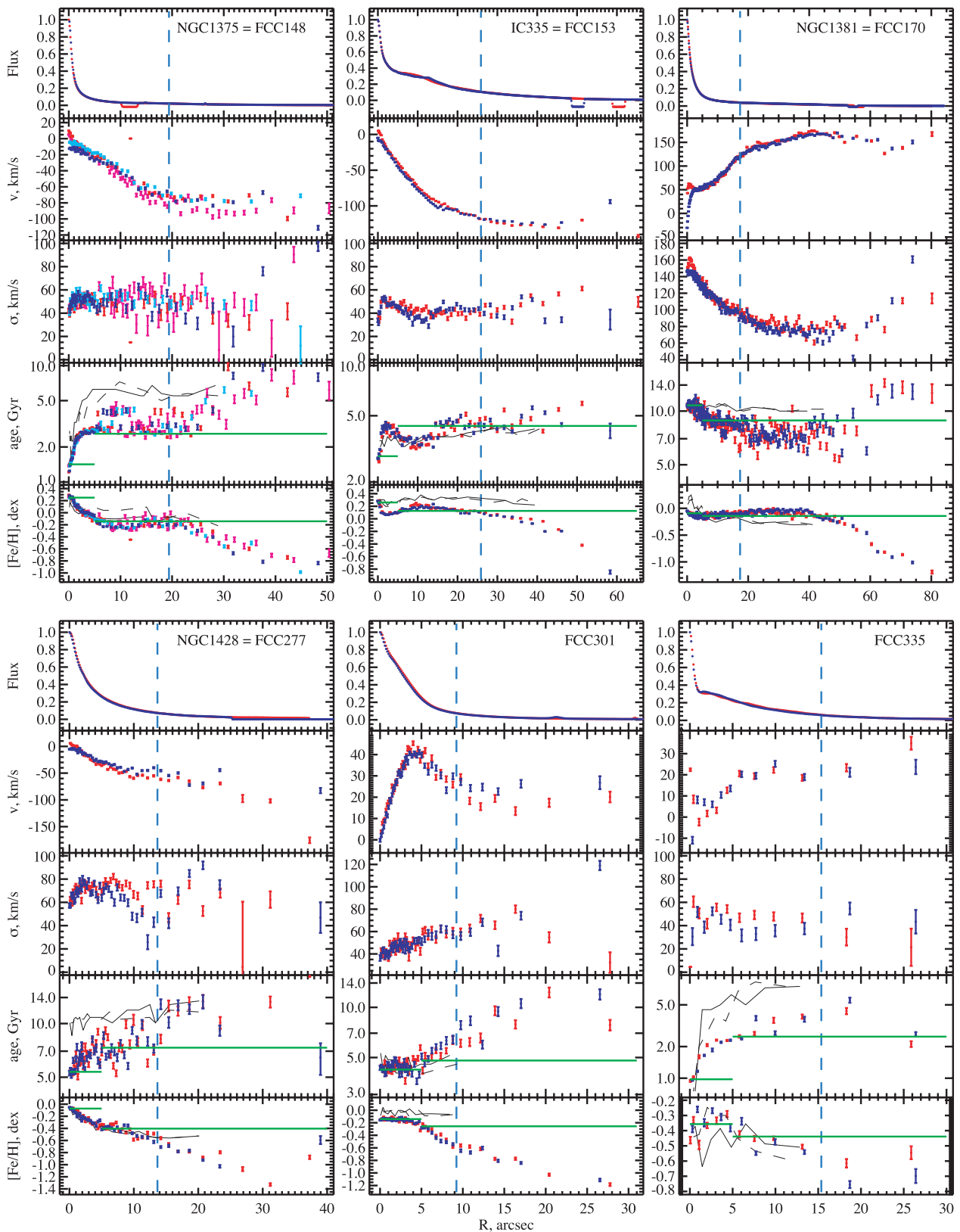
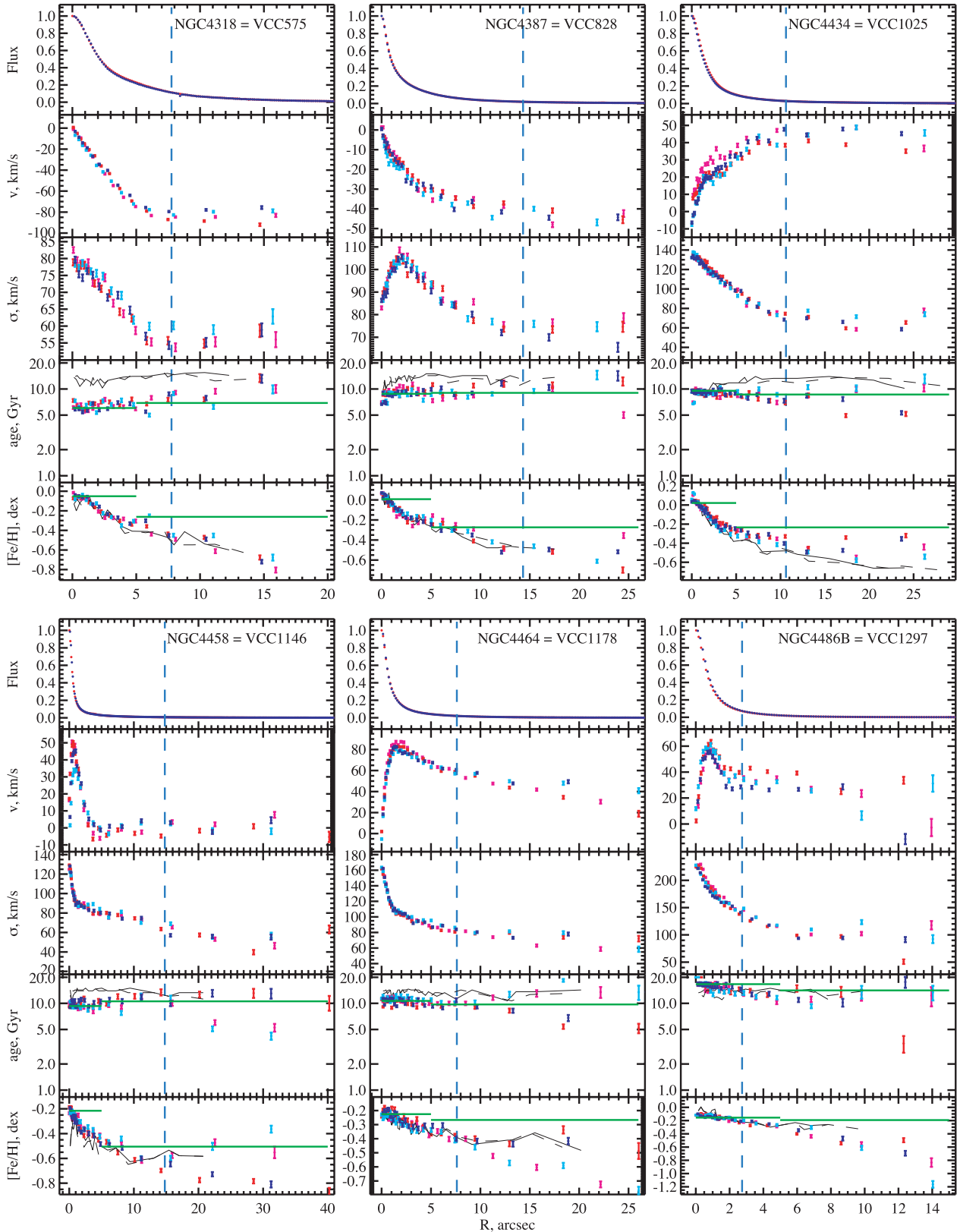


Figure 1. Radial profiles of Fornax cluster galaxies from the GMOS observations derived from SSP fits. The spectra are radially binned for a compromise between S/N and spatial resolution. The profiles are folded around the luminosity peak; the red points are for the positive radii and blue for negative (see Section 3.3). The semimajor axis of the effective isophotes is figured as vertical blue dashed lines. The SSP-equivalent metallicities and ages within the core and $1 r_{\text{eff}}$ extractions (Section 3.2) are shown with green lines (for readability they are arbitrarily drawn from 0 to 5 arcsec and from 5 arcsec outwards). The profiles drawn in black are taken from figs 1–3 of Spolaor et al. (2010b).

Figure 1 – *continued*

spectra interpolated at metallicities between those of the grid were compared with those computed by Pégase.HR using its internal interpolation. Here, we performed another test. We generated a grid of models, where the solar metallicity was removed (the neighbour-

ing metallicities are -0.4 and $+0.4$ dex). We used these models as a grid in ULYSS to determine the population parameters of solar metallicity models. We recovered the metallicity with a precision of about 0.03 dex (4 per cents of the mesh size) and the ages to about

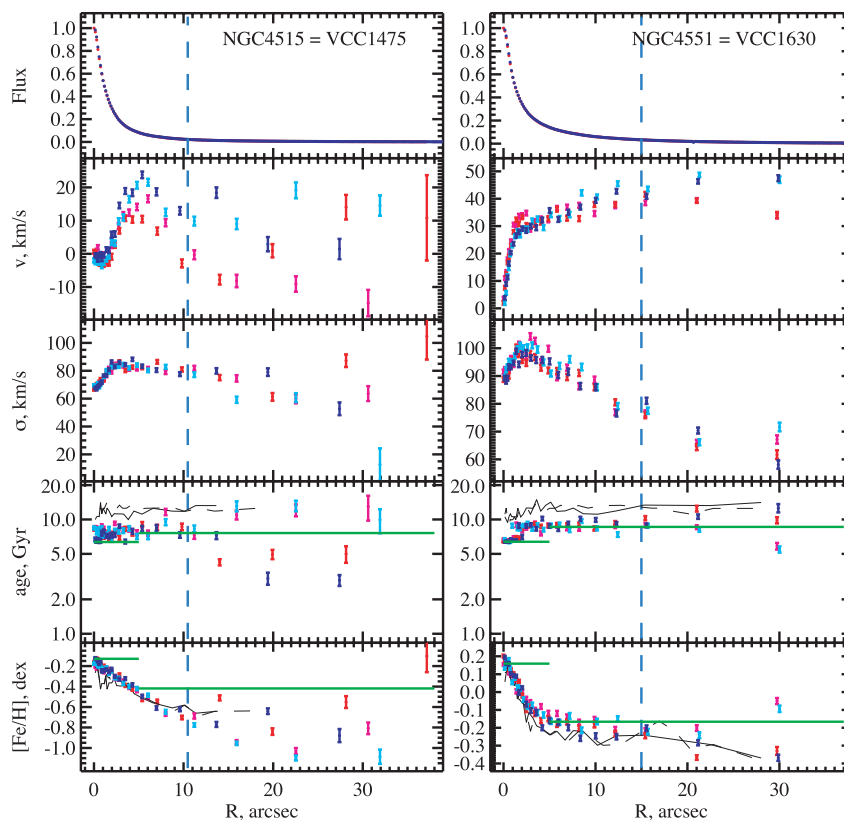


Figure 1 – continued

0.1 dex. Therefore, the precision of the interpolation shall not affect the gradients by more than those values.

4 COMPARISON WITH THE LITERATURE

4.1 Comparison with Spolaor et al.

One of the goals of this study is to shed some light on the apparent discrepancy between Spolaor et al. (2009, 2010b) and our own previous measurements (Koleva et al. 2009a). The former study finds a tight relation between the luminosity or velocity dispersion and the metallicity gradients, while the latter does not find any relation. These two papers are based on different samples and use different methods, and whether the cause of the discrepancy resides in the sample selection, bias in the method or data processing could not be clarified before.

A tight relation between the mass and the metallicity gradients is not immediately expected. First, it could not be anticipated from any earlier studies, and, secondly, since the sample is a mix of morphologies, it would imply a new and very general scaling relation. In addition, the evolution, through environmental effects, should increase the spread, in particular for the low-mass galaxies.

We re-analysed the data used in Spolaor et al. (2009), and we compare the profiles and the gradients of age and metallicity obtained in both studies.

4.1.1 Comparison of the profiles

We digitized the profiles from figs 1–3 of Spolaor et al. (2010b) and checked that this process did not introduce significant errors. We converted the total metallicity into $[\text{Fe}/\text{H}]$ as: $[\text{Fe}/\text{H}] =$

$[\text{Z}/\text{H}] - 0.94 [\alpha/\text{Fe}]$ (Thomas, Maraston & Bender 2003, hereafter TMB), consistently with the models used in the source paper. We overplotted these age and metallicity profiles in Fig. 1.

We first remark that our profiles are extending to larger galactocentric distances. The reason is certainly that our method is more sensitive (as it uses all the information in the signal). Looking more closely, we see that while our Virgo profiles are going typically 1.5 times farther, those of the Fornax galaxies go twice farther. This difference between the two sub-samples may come from the fact that in the case of Fornax we co-added the individual exposures, while we kept them separated for Virgo (the wavelength setups were different and we wished to avoid an additional step in the reduction and one more source of uncertainty).

The agreement between the metallicity profiles of the Virgo galaxies is remarkably good, despite the differences in the data processing, analysis and stellar population models. The ages from Spolaor et al. (2010b) are in general older by ~ 0.1 dex (the maximum discrepancy is ~ 0.2 dex). This reflects physical differences in the population models, and in particular in the isochrones of the stellar evolution. These systematics will not be discussed further here, and we note that the shape of the profiles are similar (i.e. the relative ages are in agreement).

For the Fornax galaxies the agreement in the age and metallicity profiles is satisfactory, but we note deviations that exceed the error bars for almost all the galaxies. The clearest case is FCC 301, where Spolaor et al. (2010b) give a flat metallicity profile while our analysis reveals a gradient extending up to $3 a_{\text{eff}}$.

The reasons for these discrepancies are not clear. We may suspect the fact that Spolaor et al. measured the total metallicity and the α -elements enhancement, while we measure only the Fe metallicity. However, for the Virgo galaxies, for which the two analyses agree,

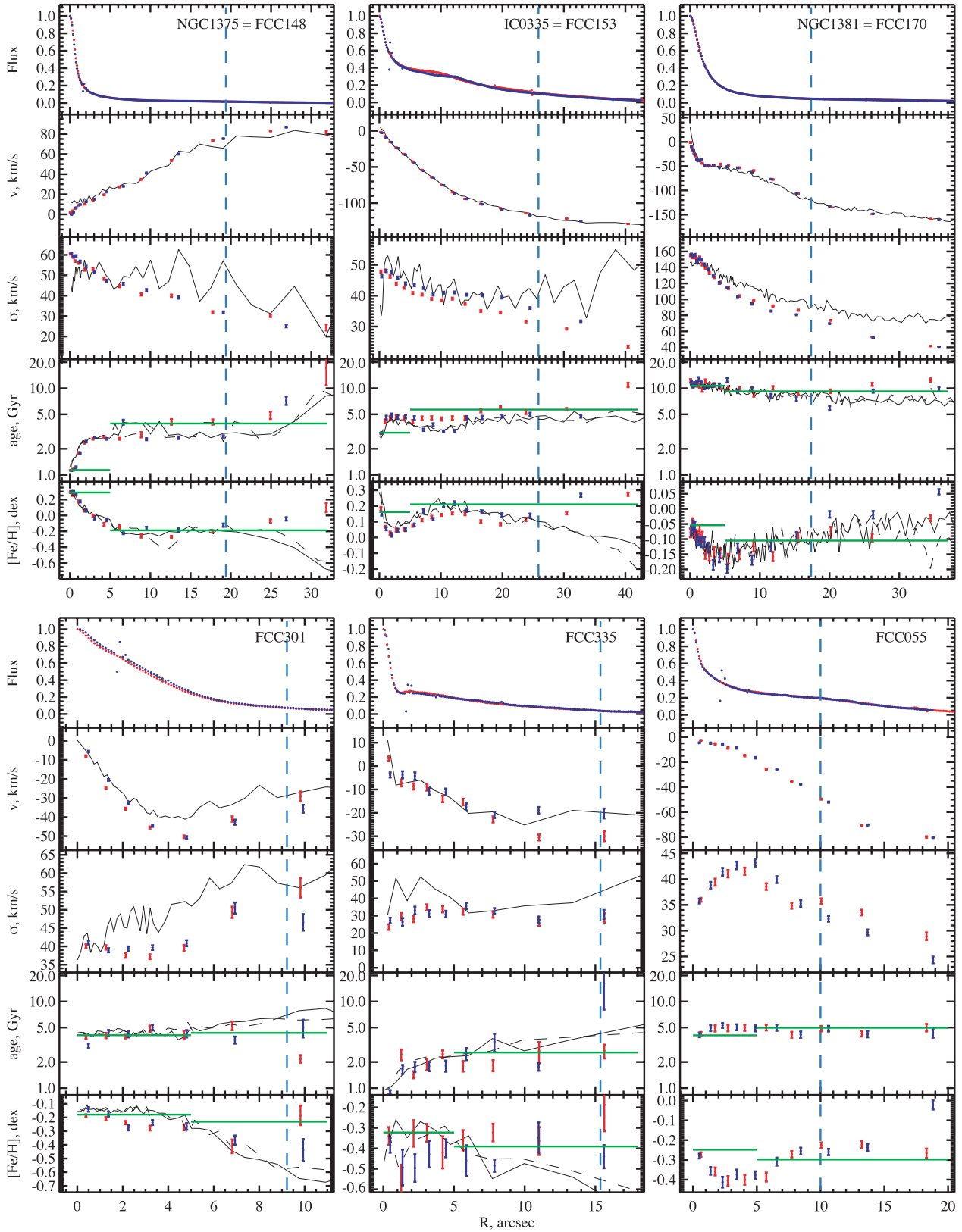


Figure 2. Radial profiles of Fornax cluster galaxies from the FORS observations. The radial binning of the spectra and the figure caption are the same as for Fig. 1. The profiles drawn in black are those from the GMOS observations presented in Fig. 1.

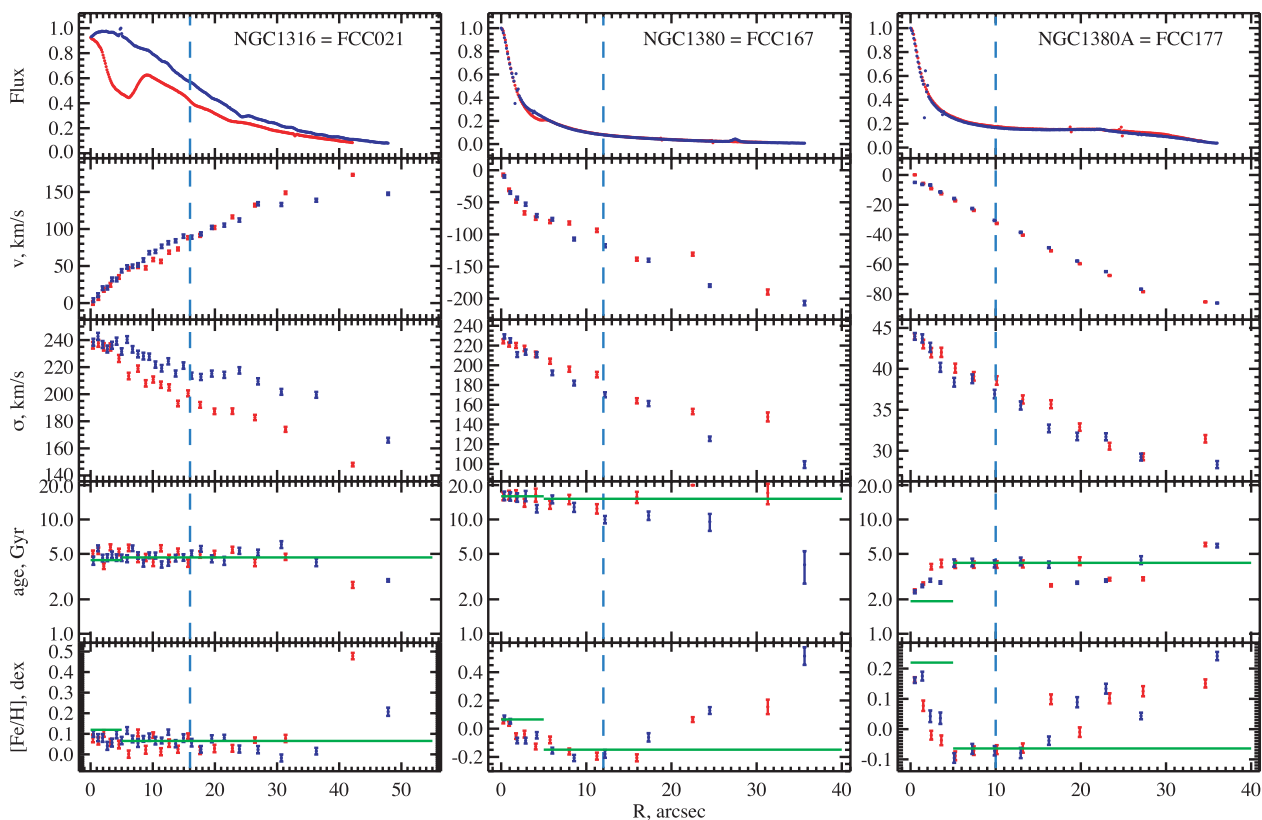


Figure 2 – continued

the populations are often α -enhanced, while they are not in the Fornax sub-sample. Still, because of degeneracies, our [Fe/H] could be biased. Nevertheless, the degeneracy between the [Fe/H] and $[\alpha/\text{Fe}]$ was examined in Koleva et al. (2008a, see also Prugniel et al., in preparation) who concluded that they are fairly decoupled. In addition, in the case of FCC 170, Spolaor et al. do not detect any enhancement, while our central fit clearly shows one (Fig. B2), confirmed by Bedregal et al. (2008) and Arrigoni et al. (2010).

On the basis of the good consistency for the Virgo galaxies, notwithstanding an age offset, and of the agreement between our analyses of the GMOS and FORS data for the Fornax galaxies, we tend to be satisfied by this comparison and trust our measurements.

4.1.2 Comparison of the gradients

Spolaor et al. used the same definition as used by us to measure the gradients. Power-law profiles are fitted between the seeing disc and the effective radius.

However, the comparison between our gradients and their values is not consistent, even for the Virgo sub-sample for which the profiles agree. A quick check for one of the discrepant Virgo galaxies, VCC 575, reveals the possible explanation. The hand fit of the profile in their fig. 2, considering the points between the seeing disc (marked on the graphic) and the effective radius, indicates a total metallicity gradient of about -0.3 , while their tabulated result is -0.11 . The tabulated value may possibly be reproduced if the central points, within the seeing disc, are included. To check our initial guess that the discrepancy may result from the erroneous inclusion of the central region, we performed unweighted linear fit of all the Spolaor et al. profiles. We present in Fig. 12 the profiles for FCC 148 and VCC 575, together with their and our fits to their data, using

the radial range between the seeing disc and the effective semimajor axis. Our new fits are generally in good agreement with the fits of our own profiles. However, another hypothesis shall be examined: Spolaor et al. fits are weighed by the errors on individual points, while our test is based on unweighted fits (the individual errors in Spolaor et al. are not available). The data were binned together to reach a minimal $S/N/\text{\AA}$ of 35 (near 5200 \AA), and while the error bars should be nearly constant for most of the body of the galaxies, the core region has in some cases smaller errors. Nevertheless, this overweighted region is in general within the seeing disc. Therefore, the variation of the weight cannot explain the divergence. A close look at the profile of FCC 148 (Fig. 12) shows that it is not possible to reproduce the fit of Spolaor et al. simply by adapting the weight of each point. Thus, we tend to believe that the authors did not exclude the points in the seeing disc. The exclusion of the central region has two strong justifications: (i) the observed profiles are not resolved within seeing disc and are expected to flatten and (ii) the power-law representation does not physically hold at small radii (i.e. it diverges). Some of the gradients derived in Spolaor et al. may therefore be erroneous.

4.2 Comparison with Sanchez-Blazquez et al.

Sánchez-Blázquez et al. (2007) analysed KECK observations of 11 early-type galaxies with $-17 \text{ mag} < M_B < -22.4 \text{ mag}$. The data have a wavelength coverage of $3110\text{--}5617 \text{ \AA}$ and a resolution of 8 \AA . They measured 19 line strength indices up to $2 r_{\text{eff}}$. As in Spolaor et al. (2009, 2010b), they used the χ^2 minimization technique described in Proctor & Sansom (2002) and two different population models, a preliminary version of Vazdekis et al. (2010) and TMB.

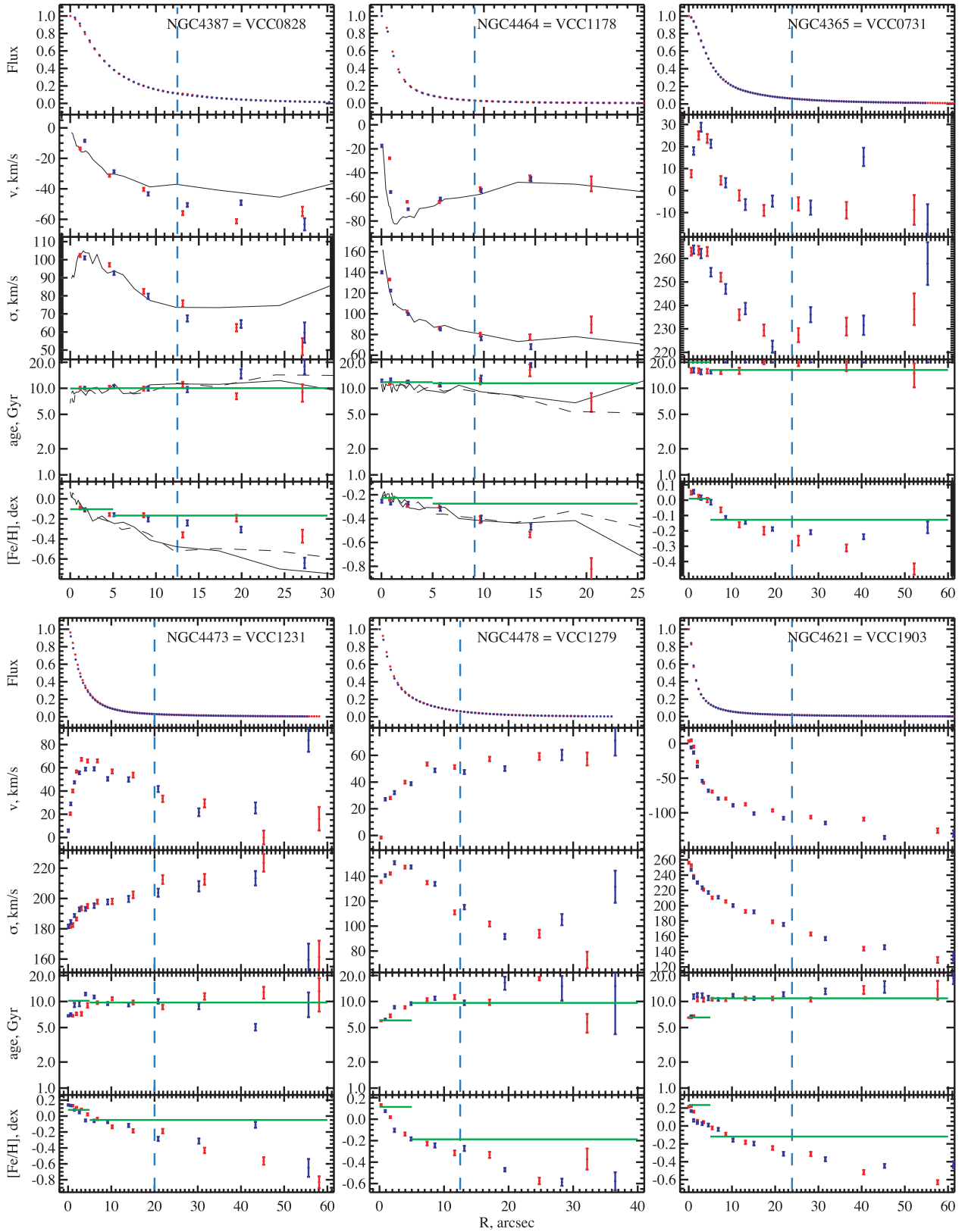


Figure 3. Radial profiles of the Virgo galaxies of the VAKU sample. The radial binning of the spectra and the figure caption are the same as for Fig. 1. The profiles drawn in black are those from the GMOS observations presented in Fig. 1.

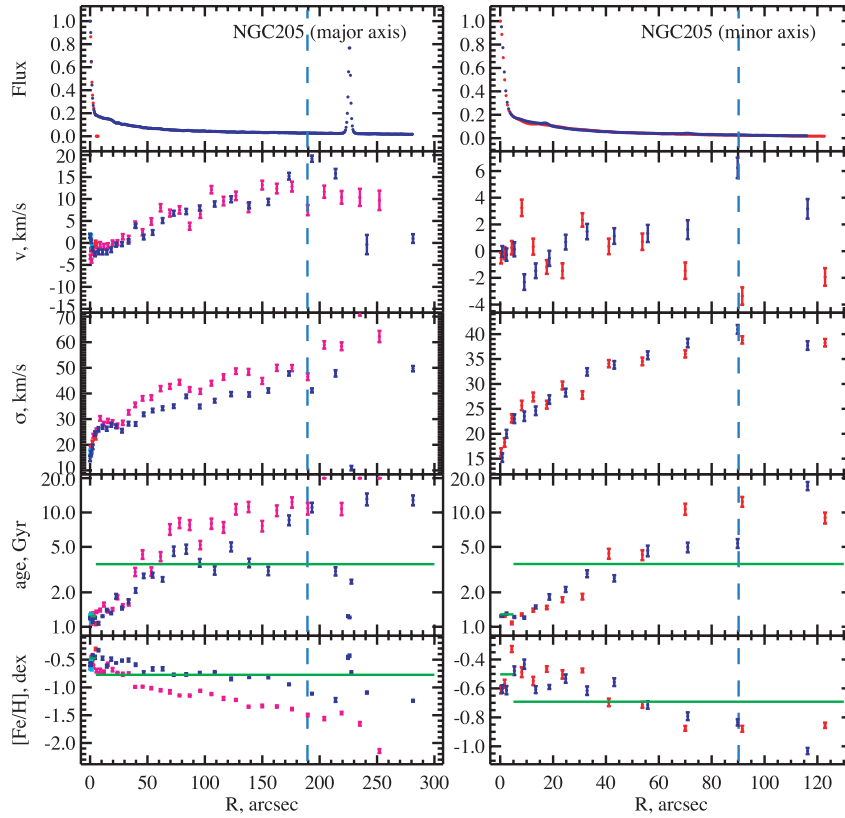


Figure 4. Radial profiles for NGC 205. The radial binning of the spectra and the figure caption are the same as for Fig. 1.

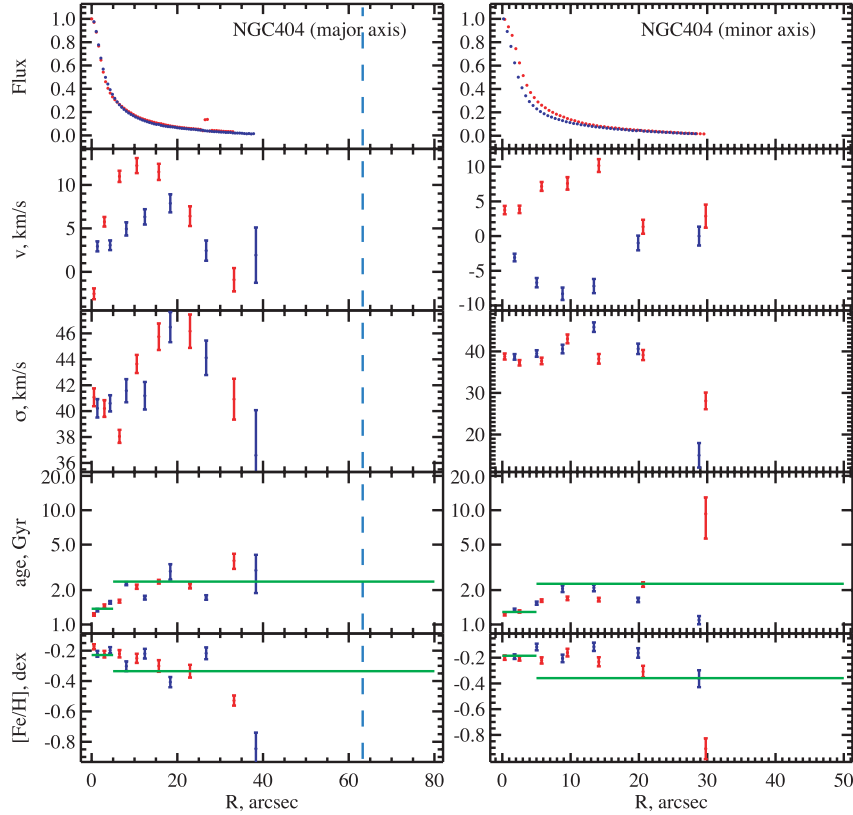


Figure 5. Radial profiles for NGC 404. The radial binning of the spectra and the figure caption are the same as for Fig. 1.

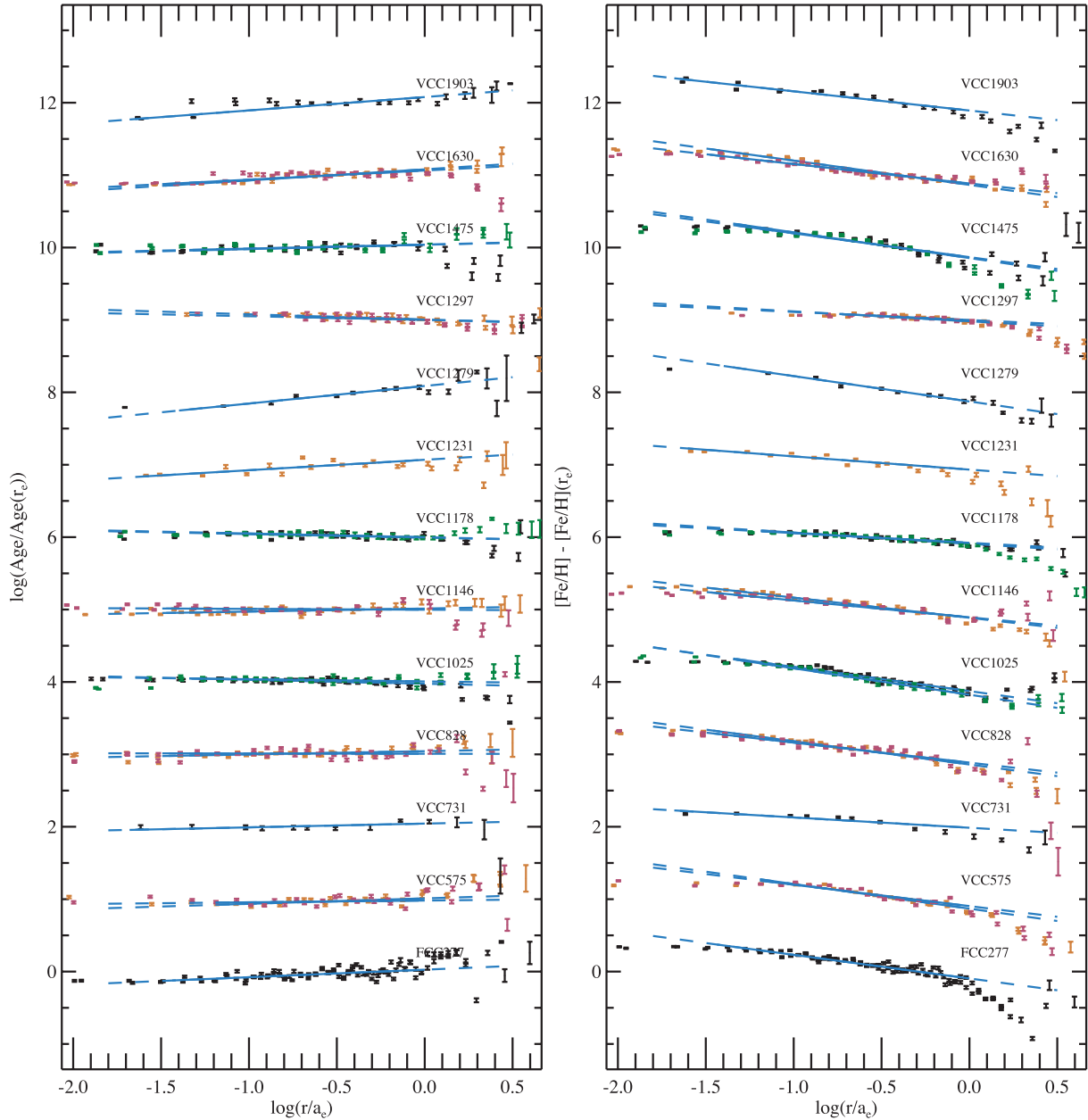


Figure 6. Radial gradients of ages and metallicity for the elliptical galaxies. The age profiles are shown on the left-hand panel, and the $[\text{Fe}/\text{H}]$ ones on the right one. The abscissa is the radius normalized to the semimajor effective radius (a_{eff}). The ordinates are the decimal logarithm of age (left) and metallicity (right) normalized to the effective aperture extraction. Each profile is labelled by the galaxy name and shifted by 1 dex. The blue lines are the linear fits of the gradients, and the continuous sections represent the region used for the fit (1 arcsec to $1 a_{\text{eff}}$), while the dashed parts extrapolate the fits to small and large values.

We have four galaxies in common with this sample: NGC 4387 = VCC 828, NGC 4458 = VCC 1146, NGC 4464 = VCC 1178 and NGC 4551 = VCC 1630. The comparison between the gradients given by Spolaor et al. (2010b), Sánchez-Blázquez et al. (2007) and our measurements is given in Table 6. For Sánchez-Blázquez et al. (2007), we used the 19 indices and TMB models to closely match the analyses made by Spolaor et al. (2010b). To compare the $[\text{Z}/\text{H}]$ measurements with our of $\nabla_{\text{Fe}/\text{H}}$ we use the $[\text{Fe}/\text{H}] = [\text{Z}/\text{H}] - 0.94 [\alpha/\text{Fe}]$. All of our measurements are consistent with those from Sánchez-Blázquez et al. (2007) within the error bars.

4.3 Comparison with Bedregal et al.

Five of the six Fornax galaxies observed with GMOS were observed by Bedregal et al. (2006) with FORS, with higher spectral resolution, but with lower S/N. We processed and analysed the data from both instruments and compared the results (Fig. 2). The consistency is more than satisfactory, so we do not expect any bias in the radial profiles due to the data processing.

Bedregal et al. (2008, 2011) also performed stellar population analyses of their sample using 10 line strengths (with different combinations to derive Fe, $[\text{MgFe}]'$ and age) and Bruzual & Charlot

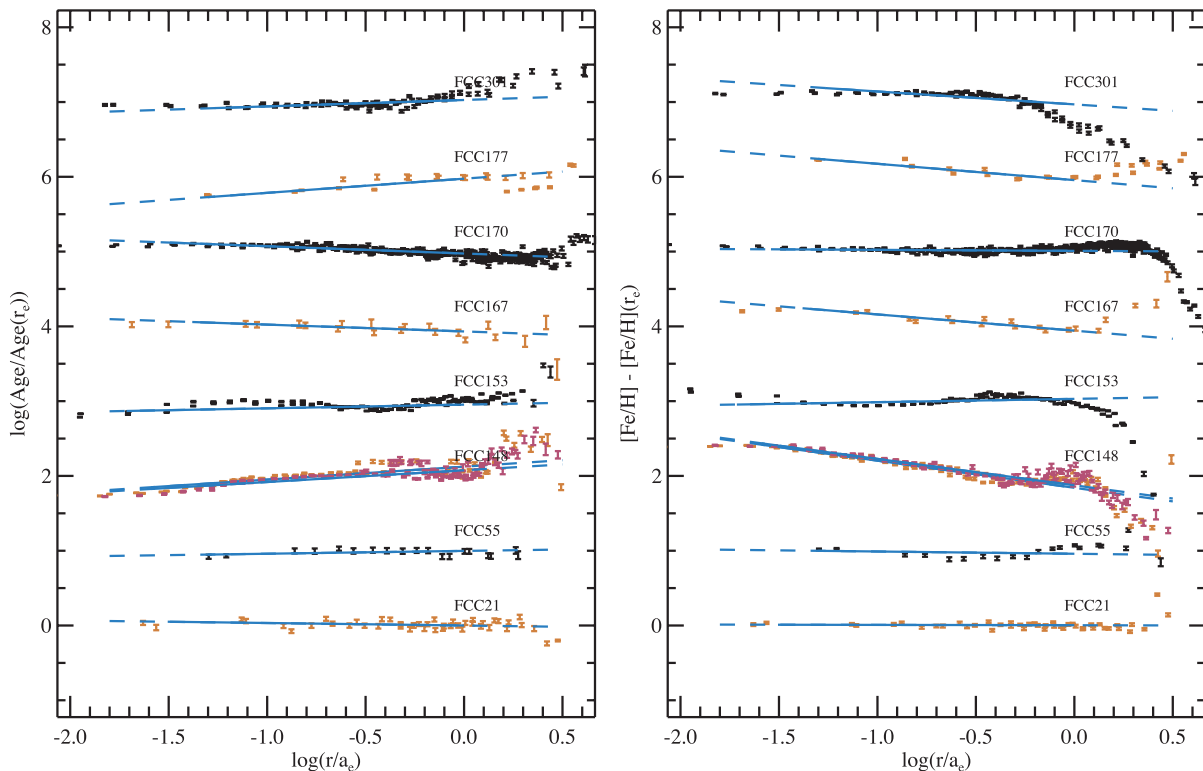


Figure 7. Radial gradients of ages and metallicity for the S0 galaxies. Same conventions as for Fig. 6.

(2003) and Vazdekis et al. (2010) models. Their age and metallicity measurements have lower precision, since they use Lick indices, but are in good agreement with ours (Koleva et al. 2011).

5 DISCUSSION

We analysed the stellar populations of 40 early-type galaxies along their major axis (and also along the minor axis for NGC 205 and 404) up to one to three times the effective radius. The sample mixes various morphologies of galaxies and our analysis revealed (or confirmed) a diversity of kinematical and population profiles. The individual objects are discussed in Appendix C.

In this section, we will enlarge the discussion by comparing our objects to lower mass dwarf spheroidals and to massive early-type galaxies. We include low-mass dSph/dE galaxies from the M81 and Centaurus A groups (Lianou et al. 2010; Crnojević et al. 2010). We estimated the gradients from the figures of these papers. The velocity dispersion for KDG 64 is taken from Simien & Prugniel (2002) and the age for KDG 61 and 64 from Makarova et al. (2010) (the metallicities from the Makarova et al. and Lianou et al. are in an acceptable agreement). We add the Local Group dwarf galaxies with spectroscopic measurements of a significant number of stars: Sextans (Battaglia et al. 2011), Fornax (Battaglia et al. 2006) and Sculptor (Kirby et al. 2009). We did not include Leo I as the gradients determined by Gullieuszik et al. (2009) are based on fewer stars. For Sextans and Sculptor, the effective radius and luminosity were taken from Irwin & Hatzidimitriou (1995) and Walker et al. (2010). The velocity dispersion of the Local Group galaxies is from HyperLeda. Finally, we also consider samples of more massive, early-type, cluster galaxies presented in Sánchez-Blázquez et al. (2007) and Rawle et al. (2010).

We will first locate our sample in the general mass versus metallicity and age relations. Then, we will discuss the systematics of the profiles and of the gradients, and will examine the distribution of the gradients as a function of the mass and of other characteristics.

5.1 Mass–metallicity and mass–age relations

In Fig. 13, we show the relations between the central metallicity and age, and absolute B -band luminosity and central velocity dispersion. There is a clear rising trend of central metallicity with luminosity and velocity dispersion; an example of the well-known mass–metallicity relation (e.g. Henry & Worthey 1999). Likewise, central age increases with luminosity and velocity dispersion. This is an example of *downsizing* (Cowie et al. 1996). While these trends appear rather continuous, we cannot exclude the possibility of a discontinuity, or at least of a slope change, between the dSphs and the more massive galaxies. In the luminosity *versus* metallicity relation, this discontinuity would be about 0.5 dex at $M_B \approx -15$ mag, the dSphs being less metallic than the extrapolation of the relation derived from the more massive galaxies. However, the metallicity is derived using different methods for the two groups. For the dSphs, it is rather a mass-weighted value, while for the massive galaxies it is closer to luminosity-weighted. The difference qualitatively goes in the sense of the observed discontinuity, thus it may not be physical.

5.2 Systematics of the profiles and of the gradients

The SSP-equivalent profiles, presented in Figs 6–9 in reduced radius (r/r_{eff}), reveal some general trends. The mean gradients for each class of galaxies are reported in Table 5.

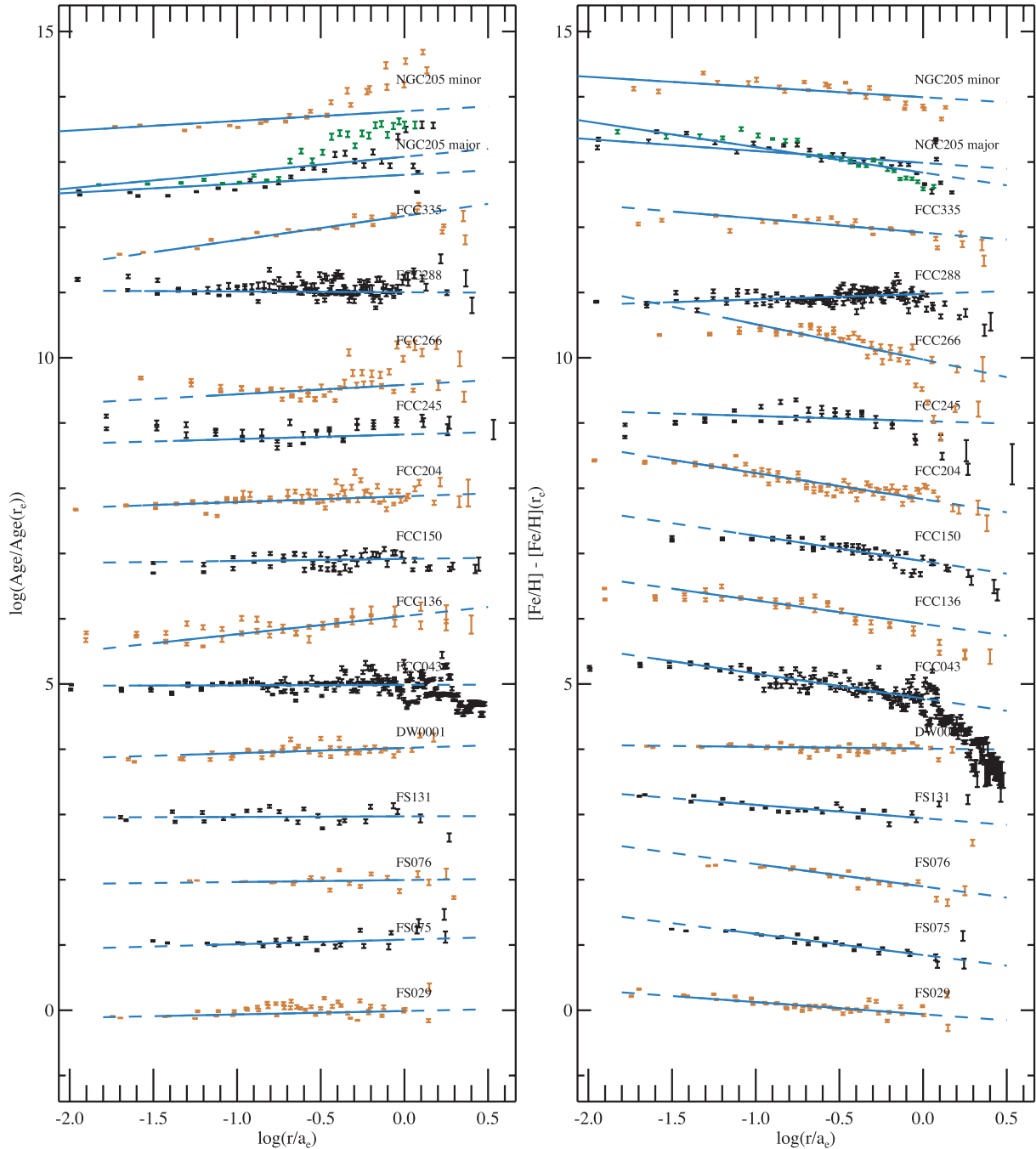


Figure 8. Radial gradients of ages and metallicity for the dE/dS0 galaxies. Same conventions as for Fig. 6.

The elliptical galaxies presented in Fig. 6 have mild and generally positive age gradients ($\langle \nabla \log(\text{Age}) \rangle = 0.06$). The only exception is VCC 1297 = NGC 4486B, the compact elliptical companion of M87. Such negative age gradient $\nabla \log(\text{Age}) = -0.10$ is rare for Es, but may be shared by other cEs (Chilingarian & Bergond 2010, see Appendix C). The metallicity gradients of the Es are in general negative, dispersed around -0.26 ± 0.08 . This is consistent with other earlier studies (e.g. Sánchez-Blázquez et al. 2006a, and the references therein). Both monolithic collapse and hierarchical structure formation (merger scenario) can explain the diversity of population radial distribution in Es (White 1980; Pipino et al. 2010).

In general, the metallicity profiles of our S0 galaxies (Fig. 7) are flatter than those of the ellipticals (dispersed around $\langle \nabla [\text{Fe}/\text{H}] \rangle \approx -0.12$). However, we observe steepening in the external regions (probably in the disc-dominated region). The age gradients are often slightly negative (note that when we consider the full errors, column 5 of Table 4, the negative age gradients are not detected in 1σ). We notice that a simple linear relation does not fit well the age and metallicity profiles of the S0s.

The gradients in age of dEs/dS0s (Fig. 8) are in general flat or increasing, but they can be much steeper than the gradients in the bigger galaxies (Es/S0s) (up to $\nabla_{\text{Age}} = +0.3$ for FCC 245, FCC 266 and FCC 335). The mean value of the age gradient in dEs/dS0s is

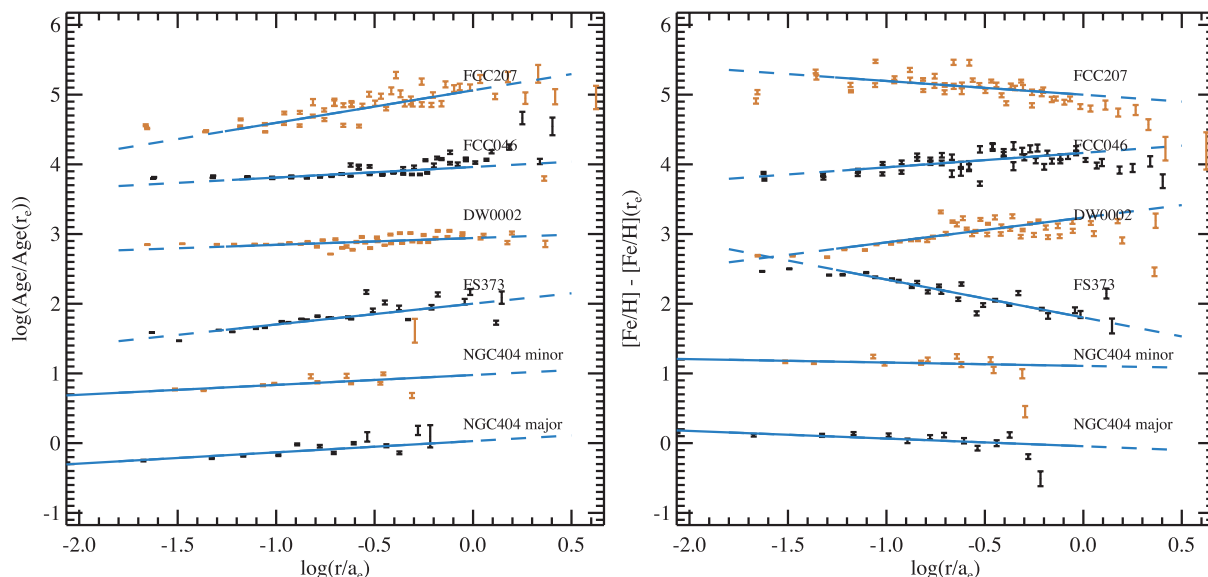


Figure 9. Radial gradients of ages and metallicity for the TTD galaxies. Same conventions as for Fig. 6.

Table 5. Mean characteristics of the sub-samples. The first column identifies the sub-sample and the second is its number of objects. The columns labelled (1) give the mean and those labelled (2) the standard deviation.

Sample	n	M_B		σ_0 (km s^{-1})		$\log \text{Age}_0$ (Myr)		$[\text{Fe}/\text{H}]_0$		∇_{Age}		$\nabla_{[\text{Fe}/\text{H}]}$	
		(1)	(2)	(1)	(2)	(1)	(2)	(1)	(2)	(1)	(2)	(1)	(2)
Our full sample	40	-17.66	1.52	93	59	3.62	0.34	-0.15	0.31	0.09	0.13	-0.21	0.18
E	13	-18.50	1.09	139	51	3.94	0.16	-0.02	0.14	0.06	0.09	-0.26	0.08
S0	8	-19.01	1.56	113	70	3.63	0.33	0.05	0.18	0.01	0.11	-0.12	0.13
dE/dS0	14	-16.57	0.63	53	14	3.50	0.20	-0.24	0.27	0.10	0.14	-0.26	0.16
TTD	5	-16.34	0.82	53	15	3.13	0.07	-0.54	0.42	0.24	0.11	-0.06	0.32
dSph (literature)	17	-11.69	1.18	12	7	3.42	0.19	-1.39	0.19			-0.10	0.12

0.10 with a cosmic spread of 0.14 (standard deviation), while for Es and S0s the dispersion is 0.10. The metallicity gradient variation is also quite prominent, with a mean value of -0.26 and a dispersion of 0.16. For some of the galaxies (FCC 043, FCC 266, FCC 288, NGC 205) we notice the same metallicity behaviour as for the S0s – almost flat profile in the beginning and steeply decreasing after $\sim 1 a_{\text{eff}}$. In most of the cases the age is opposite to the metallicity gradient which may translate into flat colour gradients. This is confirmed by a simple test: we computed a set of colour gradients⁶ for FCC 335 and found that their values are spread around 0.03 mag per $1 a_{\text{eff}}$, i.e. of the order of the photometric errors.

Our five TTD galaxies have strong positive age gradients ($\langle \nabla_{\text{Age}} \rangle = +0.24$). The metallicity gradients of FCC 046 and DW2 are also positive, while for the rest it is flat to negative.

We notice that the gradient of the minor axes for NGC 205 and 404 does not differ from those of their major axes. Thus, these galaxies seem to have a central (as opposite to axial) symmetry.

5.3 Gradients versus mass

In Fig. 14, we plot the gradients versus the B -band luminosity. In a wide range of magnitudes ($-22 \text{ mag} < M_B < -9 \text{ mag}$) we do not observe any correlation between metallicity gradient and luminosity

(or mass, if we assume constant mass-to-light ratio). For all masses, the metallicity gradients show a wide spread in the range $-0.5 < \nabla_{[\text{Fe}/\text{H}]} < +0.1$. The most extreme metallicity gradient is observed in FCC 266 ($\nabla_{[\text{Fe}/\text{H}]} = -0.54$), but, as seen in Fig. 7, its profile does not follow the power-law model, and this large gradient may not be fully representative.

For the faintest galaxies in our sample, with $M_B \gtrsim -17$, the age gradient appears to become more positive with decreasing luminosity. In other words, the galaxy centre is increasingly younger than the outskirts in fainter galaxies. This indicates that star formation persists over longer time-scales in their inner regions than in their outskirts or that later star formation events in the smallest dwarf galaxies occur closer to the galaxy centre (Valcke, de Rijcke & Dejonghe 2008; Koleva et al. 2009a). In massive ellipticals, the age gradient shows a wide spread in the range $-0.2 < \nabla_{\text{Age}} < +0.4$. On average, the galaxies have negative metallicity gradients ($\langle \nabla_{[\text{Fe}/\text{H}]} \rangle = -0.2$) and positive age gradients ($\langle \nabla_{\text{Age}} \rangle = 0.09$) over the whole mass range. Replacing M_B with σ_0 yields the same conclusion.

The tight relation presented by Spolaor et al. (2009) is not consistent with the strong gradients found in the Local Group dSph galaxies and is not confirmed by our present study. To support their empirical result, Spolaor et al. (2009) mention the concordance with the results of SPH simulations with collapse and feedback by Kawata & Gibson (2003). These latter authors computed three models of different masses, tuning the feedback parameters in order

⁶ In several photometric bands, from U to K using miles.iac.es web tools.

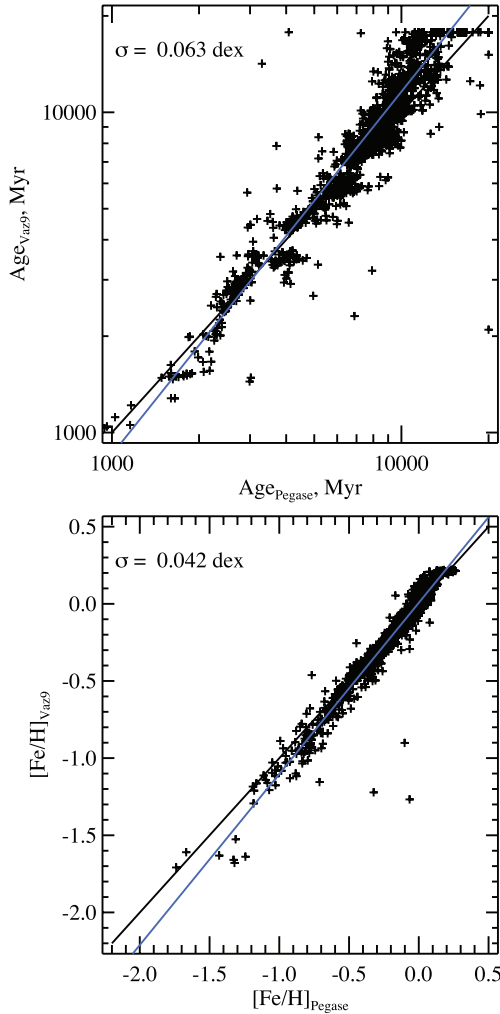


Figure 10. Comparison between the SSP analysis with the Vazdekis 9 models and with the Pegase.HR models based on the ELODIE 3.1 library for the GMOS data. The residual dispersions, σ , labelled on each panel are the dispersions of $\log(\text{Age})$ and $[\text{Fe}/\text{H}]$ in dex. The blue line is a linear fit to the data, and the black one is the one-to-one ratio.

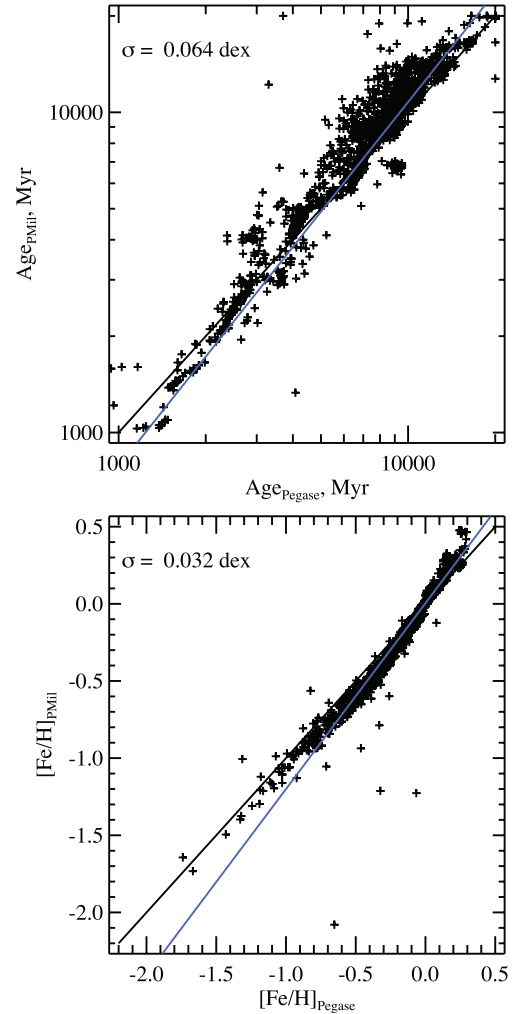


Figure 11. Comparison between the SSP analysis with Pegase.HR models based on the MILES library (preliminary unpublished version) and the ELODIE.3.1 library for the GMOS data. The lines are the same as in Fig. 10.

to match the colour–luminosity relation. The lowest mass model, corresponding to $M_B = -17$ mag, displays an homogeneous metallicity. However, its star formation was quenched too early (at $z = 1.7$) and the yield is unrealistically overabundant in α elements ($[\text{Mg}/\text{Fe}] = 0.14$) to be representative of the observed low-mass galaxies (see Michielsen et al. 2007; Koleva et al. 2009a). These models have several free parameters (beside limitations due to the resolution) and the choice of the feedback parameters is certainly not a unique solution that could reproduce the colour–luminosity relation. With a similar approach but different parameters, Kawata et al. (2006) simulated a steep metallicity gradient in a low-mass galaxy similar to the Fornax dSph. Therefore, the existence of a wide variety of gradients is not incompatible with the models.

The large scatter on the relations presented so far suggests that there is another controlling factor, such as angular momentum. As discussed in Section 5.2 and shown in Table 5, the metallicity profiles of the S0 galaxies are slightly flatter than those of the E galaxies, and in Koleva et al. (2009a) we suggested that the dEs with flat metallicity profiles have a discy structure. Moreover, simulations of dwarf galaxies flattened by rotation show that angular momentum

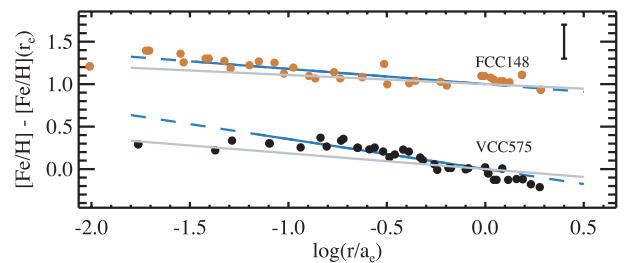


Figure 12. Comparison of the fit to the metallicity gradients. The data points are the measurements from Spolaor et al. (2010b). The grey lines are their linear fit and the blue lines ours. The dashed parts of the blue lines correspond to the excluded points, inside the 0.5 arcsec radius and outside a_{eff} . The error bar is the median error of the derived parameters.

prevents gas from rapidly sinking to the galaxy centre, thus producing dwarfs with flat metallicity profiles (Schroyen et al. 2011).

We investigate the relation of the gradients with V_{max}/σ_0 (Fig. 14). This parameter quantifies the balance between the ordered rotation and the random motions. Obviously, there is no significant trend between age or metallicity gradient and rotation. However, any

Table 6. Comparison between Sánchez-Blázquez et al. (2007), Spolaor et al. (2010b) and our data.

Galaxy	$\nabla[\text{Fe}/\text{H}]$, dex/ r_{eff}		
	Sánchez-Blázquez	Spolaor	This work
VCC 0828	-0.200 ± 0.089	-0.266 ± 0.039	-0.30 ± 0.02
VCC 1146	-0.224 ± 0.113	-0.154 ± 0.039	-0.26 ± 0.02
VCC 1178	-0.238 ± 0.065	-0.154 ± 0.039	-0.14 ± 0.02
VCC 1630	-0.334 ± 0.148	-0.269 ± 0.039	-0.30 ± 0.02

possible relation between the galaxies rotation and the gradients will be blurred by projection effects.

5.4 Gradients and central ages

The gradients versus central age diagrams are presented in Fig. 15, and Fig. 16 presents the $\nabla_{[\text{Fe}/\text{H}]}$ versus ∇_{Age} diagram.

The dwarfs with SSP-equivalent central ages younger than 4 Gyr show a statistically significant anti-correlation (95 per cent confidence level) between ∇_{Age} and Age_0 (Fig. 15). The same behaviour is observed for the S0s, while for our ‘normal ellipticals’ and the full sample of dwarfs we do not find such a trend.

Surprisingly, the statistical tests do not show any trend in the $\nabla_{[\text{Fe}/\text{H}]}$ versus Age_0 plane. Consequently, the metallicity gradient does not appear to be caused only by a young, metal-rich central stellar population. This is consistent with our findings discussed in Koleva et al. (2009a), where we presented a reconstruction of the star formation histories of a sample of dS0/dE galaxies as a function of galactocentric radius. In each radial bin, the stellar population was decomposed into different age bins using ULYSS. We found metallicity gradients to be already present in the oldest age bin, which contains stars that formed 8 to 13 Gyr ago. Moreover, our sample does not display a clear relation between $\nabla_{[\text{Fe}/\text{H}]}$ and ∇_{Age} . Such a relation is observed in the Rawle et al. (2010) data, also represented in Fig. 16. The lack of relation is consistent with the lack of relation between the metallicity and the central age. However, if we consider only the massive galaxies (Es and S0s) we can detect a trend as in Rawle et al. (2010).

It should be noted that most of the TTD galaxies have less negative, i.e. milder, metallicity gradients than dEs/dS0s at the same luminosity and that two of them have strong positive metallicity gradients (see Fig. 15). dEs/dS0s generally have extended star formation histories that were truncated more than a gigayear ago (Koleva et al. 2009a). TTD galaxies could be surmised to be the latest generation of such objects that are presently on the verge of the transformation. However, the fact that TTD galaxies belong to the rare class of early-type galaxies with an almost homogeneous metallicity may be taken as a sign that they have a different nature.

5.5 The ancestry of the quiescent dwarfs

5.5.1 Building and destroying gradients

As discussed above, simulations of the formation of dwarf galaxies show that their chemical evolution is determined by the interplay between gravity, pulling gas inwards and supernova feedback, heating and expelling gas (Valcke et al. 2008). The outcome of this interplay is that subsequent star formation events become more centrally concentrated, thus producing a positive age gradient and a negative metallicity gradient.

On the other hand, in dwarf galaxies with high specific angular momentum the centrifugal barrier prevents gas from rapidly sinking towards the potential well centre (Schroyen et al. 2011). This together with differential rotation decreases star formation efficiency. Moreover, star formation occurs galaxy-wide, as observed in dIrr (van Zee 2002), and not just near the centre. It also is more continuous and less ‘bursty’. Simulations of rotating dwarfs produce chemically homogeneous systems.

In Koleva et al. (2009a), we presented age and metallicity gradients measured in a sample of dE/dS0 galaxies. We artificially aged the stellar populations of these galaxies by 3 Gyr to mimic passive evolution and remeasured the gradients. We showed that after 3 Gyr of passive evolution the metallicity gradients are milder while the age gradients are almost completely removed. Hence, the passive evolution strongly affects the strength of the measured gradients and the general trend is to weaken them. Moreover, environmental processes that strip dwarfs from their gas, e.g. ram-pressure stripping and tidal interactions with massive galaxies, may alter the gradients as well. Any process that leads to a reshuffling of stellar orbits can be expected to weaken any existing gradients, although totally erasing them might be difficult. On the other hand, the same environmental interactions which remove gas may trigger centrally concentrated star formation by driving gas to the galaxy centre and/or compressing it. This may reinvigorate the metallicity and age gradients.

All galaxies in our sample, being gasless early-types, must have been affected by their environments (the smallest ones more so). However, we still see strong gradients in most of them. Since we find metallicity gradients also in the old stellar populations, they cannot (completely) be explained by recent star formation triggered by ram pressure and/or interactions.

5.5.2 Star forming galaxies and possible progenitors

Boselli et al. (2008) simulated ram-pressure stripping in Virgo and found that the photometric properties (colours, concentration, sizes, luminosities) of the blue compact dwarfs (BCDs) and late-type spirals are consistent with those of the cluster’s early-type dwarfs after being stripped from their gas and cessation of the star formation. They insist that even the LMC is a bit too faint to produce dwarfs with $\mu_{e,B} \sim 22$ mag arcsec², as in our sample. On the other side, van Zee (2002) predicates that the specific angular momentum of the BCDs is lower than that of similar mass dwarf irregulars. Therefore, the star formation in BCDs is stronger and more centrally concentrated (which plausibly leads to the emergence of gradients). She argues that the star formation in dIrrs is randomly distributed along the disc and that the dIrr have milder and more continuous star formation histories than BCDs.

This leads to BCDs as possible progenitors for the cluster dEs. Assuming that the BCDs are in a burst phase only for 10 Myr (e.g. Mas-Hesse & Kunth 1999), Sánchez Almeida et al. (2009) argue that they are quiet for 300 Myr. In Virgo the dEs outnumber the BCDs by a factor of 10 (Binggeli, Sandage & Tammann 1988), which leads to the conclusion that the observed number of quiescent BCDs is enough to produce the observed dEs. Sánchez Almeida et al. measured the metallicity of the gas and stars of 21493 quiescent BCDs from Sloan Digital Sky Survey and found that their mean metallicities are around -0.4 to -0.2 dex, which is consistent with the mean metallicities of early-type dwarfs. Still, as a class BCDs have a higher specific angular momentum than do dEs (van Zee, Skillman & Salzer 1998). This means that BCDs will not fade

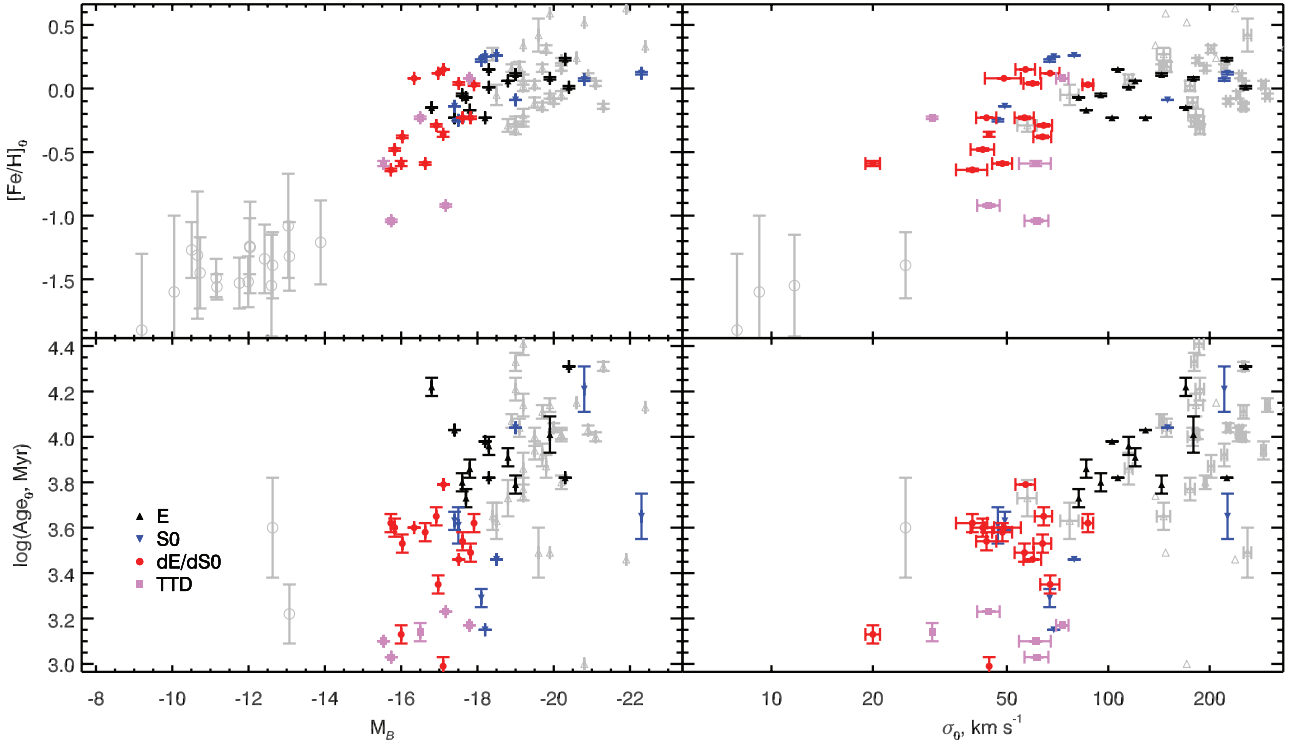


Figure 13. Central age and metallicity versus absolute magnitude and central velocity dispersion. The different classes of galaxies are represented with different colours and symbols according to the legend. The error bars are the formal fitting errors. The grey symbols are for the other galaxies compiled from the literature (see Section 5); for the dSphs, the error bars on the metallicity are the cosmic spread.

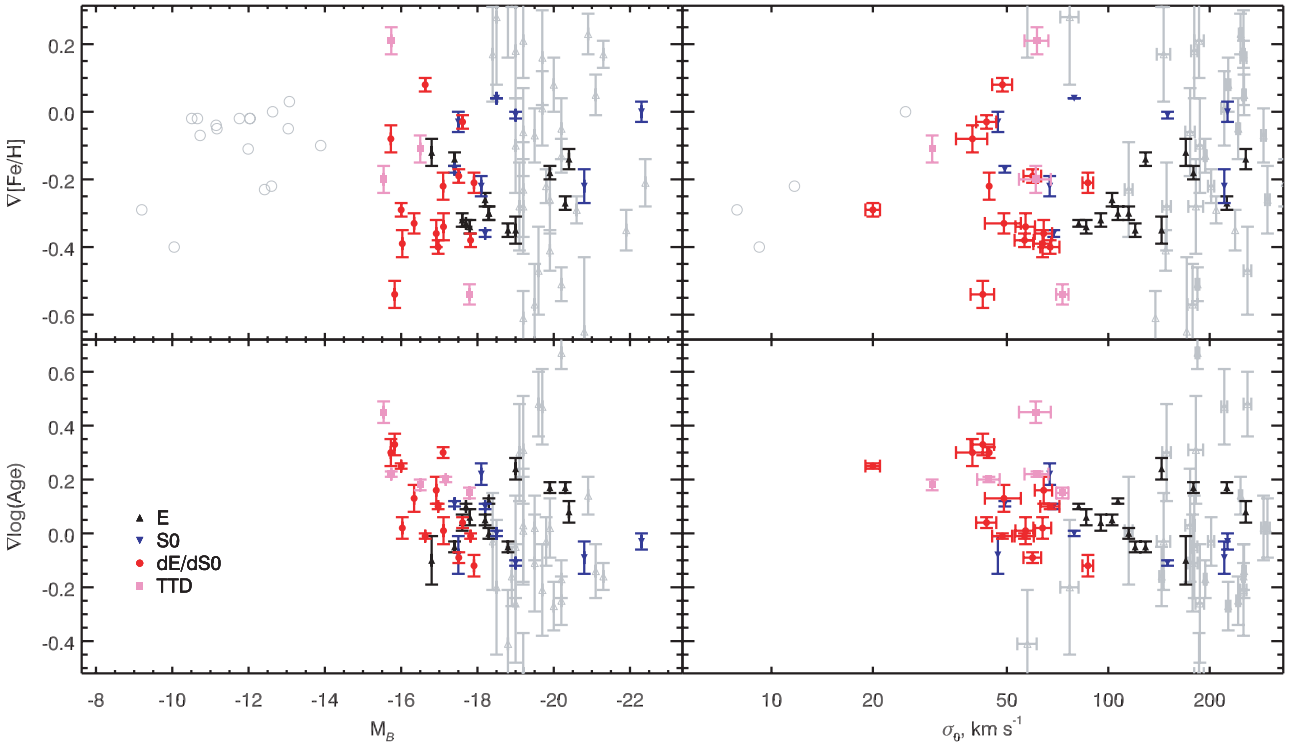


Figure 14. Gradients of age and metallicity versus absolute magnitude and central velocity dispersion. The symbols are as in Fig. 13. The dSph are represented as grey dots without error bars.

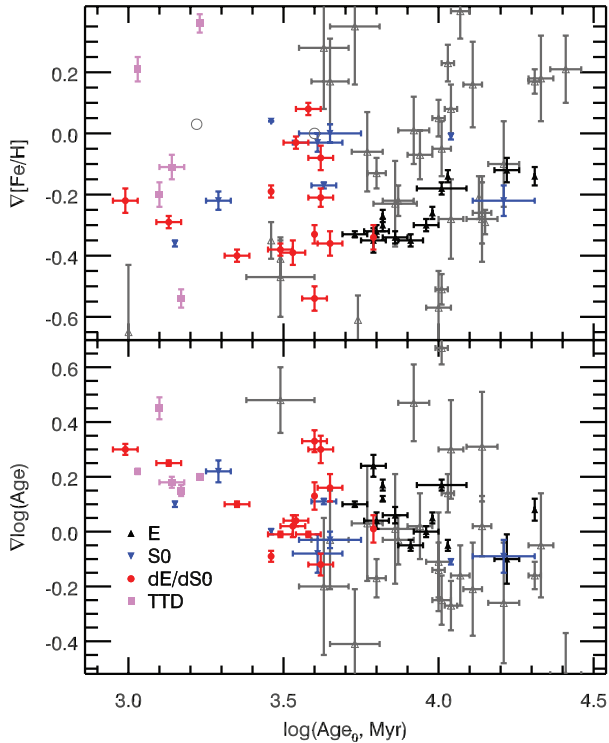


Figure 15. Gradients of age and metallicity versus central age. The symbols are as in Fig. 13.

passively into dEs after star formation has ended and that interactions with other galaxies are required to shed their angular momentum. This is in line with the observed morphology–density relation for dwarf galaxies.

Unfortunately, as mentioned before, radial studies of the stellar population in dwarf star-forming galaxies (BCDs and dIrrs) are, to our knowledge, not done up-to-date and we cannot directly compare our findings.

6 CONCLUSIONS

We analysed long slit data of 40 early-type galaxies using the full spectrum fitting code *ULYSS*. We derived the radial distribution of stellar population and kinematical characteristics. We classified the galaxies according to their morphological appearance and photometric and kinematical properties. We ended up with 14 dE/dS0, five TTD, 13 Es and eight S0s. We broadened the discussion by adding nearby dSph galaxies and massive ellipticals for which similar measurements were available in the literature.

We can summarize our main conclusions as follows.

(i) All early-type galaxies obey a metallicity–luminosity relation in the sense that less massive galaxies contain less metals. This is in agreement with previous findings.

(ii) All early-type galaxies (above $L = 10^7 \times L_{\odot}$) obey an age–luminosity relation in the sense that less massive galaxies have younger stellar populations, in an SSP sense. This is the well-known downsizing effect. It reflects the fact that the least massive galaxies continue to form stars until present, while the most massive galaxies have much shorter star formation histories.

(iii) For the massive galaxies in our sample we found that the S0s have in general milder population gradients than the Es. This may be due to the fact that angular momentum acts against building up

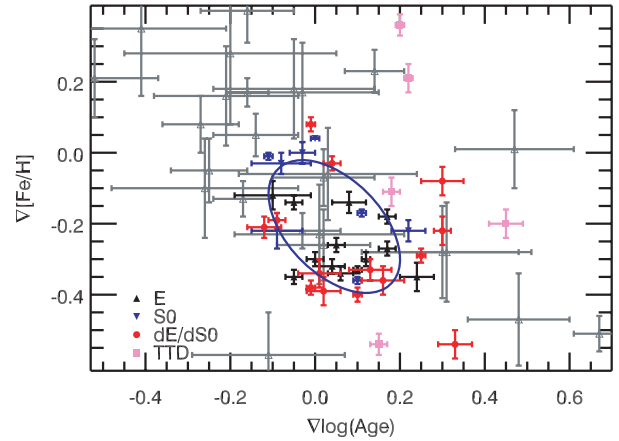


Figure 16. Gradients of age versus gradients of metallicity. The symbols are as in Fig. 13. The ellipse drawn in blue represents the covariance matrix for the E and S0 galaxies.

gradients, or simply reflects the super-position between a disc and a bulge.

(iv) We confirm previous studies where metallicity gradients were found to correlate with the age gradients, but only for giant galaxies (Es, S0s). For the dwarfs in our sample, we find no evidence for a connection between the metallicity gradient $\nabla_{\text{Fe}/\text{H}}$ and the luminosity, central age or age gradient. At every luminosity, there is a significant scatter in $\nabla_{\text{Fe}/\text{H}}$.

(v) Galaxies brighter than $M_B \sim -17$ mag show no evidence for a connection between the age gradient ∇_{Age} and any other parameter. At every luminosity, there is a significant scatter in ∇_{Age} .

(vi) Galaxies fainter than $M_B \sim -17$ mag show evidence for a relation between the age gradient ∇_{Age} and luminosity in the sense that fainter galaxies have stronger, positive age gradients. In other words, star formation persists over longer time-scales in their inner regions than in their outskirts.

(vii) Dwarf galaxies with central SSP-equivalent ages younger than 3.5 Gyr show trend of increasing ∇_{Age} when the central age decreases. This is consistent with the fact that the newly build age gradients disappear after a few Gyr of passive evolution. Due to the low, residual star formation rates, the few formed young stars are fast dissolved into the old population.

(viii) The majority of our TTD galaxies have positive or only slightly negative metallicity gradients, suggesting a different star formation efficiency than in the majority of the dEs.

We argue that low angular momentum BCDs may be the progenitors of early-type dwarfs with gradients, while high angular momentum late types, i.e. dIrrs or Sm, may be the progenitors of early-type dwarfs without gradients. In BCDs the star formation is centrally concentrated, while in discs with higher specific angular momentum it is randomly distributed (van Zee 2002). BCDs have photometric characteristics (surface brightness, effective radii, colours, the Sérsic index) similar to those of dEs after being ram-pressure stripped (Boselli et al. 2008). They also have central stellar populations (Sánchez Almeida et al. 2009) consistent with the ones of the dEs (Michielsen et al. 2007; Chilingarian 2009; Koleva et al. 2009a).

ACKNOWLEDGEMENTS

MK has been supported by the Programa Nacional de Astronomía y Astrofísica of the Spanish Ministry of Science and Innovation under

grant AYA2009-21322-C03-02. She thanks CRAL, Observatoire de Lyon, Université Claude Bernard for an Invited Professorship. PhP and WZ acknowledge a bilateral collaboration grant between France and Austria (AMADEUS, collaboration project PHC19451XM). SdR and PhP acknowledge a bilateral collaboration grant between the Flander region and France (Tournesol). We thank A. Bedregal, C. Gallart, D. Forbes, J. Sanchez-Almeida, M. Monelli and M. Fioc for useful discussions.

This work is based on observations made with ESO telescopes at Paranal observatory under programs 076.B-0196 and 70.A-0332(A); Gemini observatory under programs GS-2008A-Q-3 and GS-2006B-Q-74; Observatoire de Haute Provence (CNRS), France; archival data from WHT, La Palma, Observatorio del Roque de los Muchachos of the Instituto de Astrofísica de Canarias.

REFERENCES

- Alongi M., Bertelli G., Bressan A., Chiosi C., Fagotto F., Greggio L., Nasi E., 1993, *A&AS*, 97, 851
- Annibali F., Bressan A., Rampazzo R., Zeilinger W. W., Danese L., 2007, *A&A*, 463, 455
- Arrigoni M., Trager S. C., Somerville R. S., Gibson B. K., 2010, *MNRAS*, 402, 173
- Baade W., 1944, *ApJ*, 100, 137
- Baes M., Sil'chenko O. K., Moiseev A. V., Manakova E. A., 2007, *A&A*, 467, 991
- Battaglia G. et al., 2006, *A&A*, 459, 423
- Battaglia G., Tolstoy E., Helmi A., Irwin M., Parisi P., Hill V., Jablonka P., 2011, *MNRAS*, 411, 1013
- Bedregal A. G., Aragón-Salamanca A., Merrifield M. R., Milvang-Jensen B., 2006, *MNRAS*, 371, 1912
- Bedregal A. G., Aragón-Salamanca A., Merrifield M. R., Cardiel N., 2008, *MNRAS*, 387, 660
- Bedregal A. G., Cardiel N., Aragón-Salamanca A., Merrifield M. R., 2011, *MNRAS*, 415, 2063
- Bekki K., Shioya Y., 1999, *ApJ*, 513, 108
- Bender R., 1990, *A&A*, 229, 441
- Bender R., Paquet A., Nieto J., 1991, *A&A*, 246, 349
- Binggeli B., Sandage A., Tammann G. A., 1988, *ARA&A*, 26, 509
- Boselli A., Boissier S., Cortese L., Gavazzi G., 2008, *ApJ*, 674, 742
- Bosma A., Smith R. M., Wellington K. J., 1985, *MNRAS*, 212, 301
- Bouchard A., Prugniel P., Koleva M., Sharina M., 2010, *A&A*, 513, A54
- Bruzual G., Charlot S., 2003, *MNRAS*, 344, 1000
- Cappellari M., Bertola F., Burstein D., Buson L. M., Greggio L., Renzini A., 1999, *ApJ*, 515, L17
- Carollo C. M., Danziger I. J., Buson L., 1993, *MNRAS*, 265, 553
- Cepa J., Beckman J. E., 1988, *A&A*, 200, 21
- Chilingarian I. V., 2009, *MNRAS*, 394, 1229
- Chilingarian I. V., Bergond G., 2010, *MNRAS*, 405, L11
- Cioni M., 2009, *A&A*, 506, 1137
- Conselice C. J., O'Neil K., Gallagher J. S., Wyse R. F. G., 2003, *ApJ*, 591, 167
- Cowie L. L., Songaila A., Hu E. M., Cohen J. G., 1996, *AJ*, 112, 839
- Crnojević D., Grebel E. K., Koch A., 2010, *A&A*, 516, A85
- Davidge T. J., 1991, *AJ*, 102, 896
- Davies R. L. et al., 2001, *ApJ*, 548, L33
- De Rijcke S., Dejonghe H., Zeilinger W. W., Hau G. K. T., 2001, *ApJ*, 559, L21
- De Rijcke S., Dejonghe H., Zeilinger W. W., Hau G. K. T., 2003a, *A&A*, 400, 119
- De Rijcke S., Zeilinger W. W., Dejonghe H., Hau G. K. T., 2003b, *MNRAS*, 339, 225
- De Rijcke S., Dejonghe H., Zeilinger W. W., Hau G. K. T., 2004, *A&A*, 426, 53
- De Rijcke S., Michielsen D., Dejonghe H., Zeilinger W. W., Hau G. K. T., 2005, *A&A*, 438, 491
- De Rijcke S., Prugniel P., Simien F., Dejonghe H., 2006, *MNRAS*, 369, 1321
- de Vaucouleurs G., 1961, *ApJS*, 5, 233
- del Río M. S., Brinks E., Cepa J., 2004, *AJ*, 128, 89
- Demers S., Battinelli P., Letarte B., 2003, *AJ*, 125, 3037
- Di Matteo P., Pipino A., Lehnert M. D., Combes F., Semelin B., 2009, *A&A*, 499, 427
- di Serego Alighieri S. et al., 2007, *A&A*, 474, 851
- Feast M. W., Abedigamba O. P., Whitelock P. A., 2010, *MNRAS*, 408, L76
- Forbes D. A., Sánchez-Blázquez P., Proctor R., 2005, *MNRAS*, 361, L6
- Gallagher J. S., III, 1986, *PASP*, 98, 81
- Geha M., Guhathakurta P., Rich R. M., Cooper M. C., 2006, *AJ*, 131, 332
- Gullieuszik M., Held E. V., Saviane I., Rizzi L., 2009, *A&A*, 500, 735
- Haas M., 1998, *A&A*, 337, L1
- Halliday C., Davies R. L., Kuntschner H., Birkinshaw M., Bender R., Saglia R. P., Baggle G., 2001, *MNRAS*, 326, 473
- Harbeck D. et al., 2001, *AJ*, 122, 3092
- Henry R. B. C., Worthey G., 1999, *PASP*, 111, 919
- Ho L. C., Filippenko A. V., Sargent W. L. W., 1993, *ApJ*, 417, 63
- Hopkins P. F., Cox T. J., Dutta S. N., Hernquist L., Kormendy J., Lauer T. R., 2009, *ApJS*, 181, 135
- Irwin M., Hatzidimitriou D., 1995, *MNRAS*, 277, 1354
- Kawata D., Gibson B. K., 2003, *MNRAS*, 340, 908
- Kawata D., Arimoto N., Cen R., Gibson B. K., 2006, *ApJ*, 641, 785
- Keller S. C., Yong D., Da Costa G. S., 2010, *ApJ*, 720, 940
- Kirby E. N., Guhathakurta P., Bolte M., Sneden C., Geha M. C., 2009, *ApJ*, 705, 328
- Kleyna J. T., Wilkinson M. I., Evans N. W., Gilmore G., 2004, *MNRAS*, 354, L66
- Kobayashi C., 2004, *MNRAS*, 347, 740
- Kobulnicky H. A., Skillman E. D., 1997, *ApJ*, 489, 636
- Koleva M., 2009, PhD thesis, University of Lyon
- Koleva M., Bavouzet N., Chilingarian I., Prugniel P., 2007, in Kissler-Patig M., Walsh J. R., Roth M. M., eds, *Science Perspectives for 3D Spectroscopy*. Springer, Garching, p. 153
- Koleva M., Gupta R., Prugniel P., Singh H., 2008a, in Knapen J. H., Mahoney T. J., Vazdekis A., eds, *ASP Conf. Ser. Vol. 390, Pathways Through an Eclectic Universe*. Astron. Soc. Pac., San Francisco, p. 302
- Koleva M., Prugniel P., Ocvirk P., Le Borgne D., Soubiran C., 2008b, *MNRAS*, 385, 1998
- Koleva M., de Rijcke S., Prugniel P., Zeilinger W. W., Michielsen D., 2009a, *MNRAS*, 396, 2133
- Koleva M., Prugniel P., Bouchard A., Wu Y., 2009b, *A&A*, 501, 1269
- Koleva M., Prugniel P., De Rijcke S., Zeilinger W. W., Michielsen D., 2009c, *Astron. Nachr.*, 330, 960
- Koleva M., Bedregal A., Prugniel P., De Rijcke S., Zeilinger W. W., 2011, in Koleva M., Prugniel P., Vauglin I., eds, *EAS Publ. Ser. Vol. 48, CRAL-2010: A Universe of Dwarf Galaxies*. EDP Sciences, Les Ulis, p. 85
- Kormendy J., 1985, *ApJ*, 295, 73
- Kormendy J., 1989, *ApJ*, 342, L63
- Kormendy J. et al., 1997, *ApJ*, 482, L139
- Kormendy J., Fisher D. B., Cornell M. E., Bender R., 2009, *ApJS*, 182, 216
- Krajinović D., Jaffe W., 2004, *A&A*, 428, 877
- Kuntschner H., 2000, *MNRAS*, 315, 184
- Larson R. B., 1974, *MNRAS*, 166, 585
- Lauer T. R. et al., 1996, *ApJ*, 471, L79
- Le Borgne D., Rocca-Volmerange B., Prugniel P., Lançon A., Fioc M., Soubiran C., 2004, *A&A*, 425, 881
- Lianou S., Grebel E. K., Koch A., 2010, preprint (arXiv e-prints)
- Lisker T., Grebel E. K., Binggeli B., Glatt K., 2007, *ApJ*, 660, 1186
- McClure R. D., 1969, *AJ*, 74, 50
- Mackie G., Fabbiano G., 1998, *AJ*, 115, 514
- Makarova L., Koleva M., Makarov D., Prugniel P., 2010, *MNRAS*, 406, 1152
- Martínez-Delgado D., Gallart C., Aparicio A., 1999, *AJ*, 118, 862
- Mas-Hesse J. M., Kunth D., 1999, *A&A*, 349, 765

- Mehlert D., Thomas D., Saglia R. P., Bender R., Wegner G., 2003, *A&A*, 407, 423
- Merluzzi P., Busarello G., Terranegra L., Colless M. M., Graham A. W., 1998, *Mem. Soc. Astron. Italiana*, 69, 283
- Michielsen D., De Rijcke S., Zeilinger W. W., Prugniel P., Dejonghe H., Roberts S., 2004, *MNRAS*, 353, 1293
- Michielsen D. et al., 2007, *ApJ*, 670, L101
- Morelli L. et al., 2004, *MNRAS*, 354, 753
- Nieto J.-L., Prugniel P., 1987, *A&A*, 186, 30
- Nowak N., Saglia R. P., Thomas J., Bender R., Davies R. I., Gebhardt K., 2008, *MNRAS*, 391, 1629
- Ogando R. L. C., Maia M. A. G., Chiappini C., Pellegrini P. S., Schiavon R. P., da Costa L. N., 2005, *ApJ*, 632, L61
- Okamoto S. et al., 2008, in Kodama T., Yamada T., Aoki K., eds, *ASP Conf. Ser. Vol. 399, Panoramic Views of Galaxies Formation and Evolution*. Astron. Soc. Pac., San Francisco, p. 469
- Paturel G., Petit C., Prugniel P., Theureau G., Rousseau J., Brouty M., Dubois P., Cambr esy L., 2003, *A&A*, 412, 45
- Peletier R. F., 1993, *A&A*, 271, 51
- Pinkney J. et al., 2003, *ApJ*, 596, 903
- Pipino A., D’Ercole A., Matteucci F., 2008, *A&A*, 484, 679
- Pipino A., D’Ercole A., Chiappini C., Matteucci F., 2010, *MNRAS*, 407, 1347
- Pogge R. W., Maoz D., Ho L. C., Eracleous M., 2000, *ApJ*, 532, 323
- Proctor R. N., Sansom A. E., 2002, *MNRAS*, 333, 517
- Prugniel P., 1994, in Meylan G., Prugniel P., eds, *European Southern Observatory Conference and Workshop Proceedings, Vol. 49*, p. 171
- Prugniel P., Soubiran C., 2001, *A&A*, 369, 1048
- Prugniel P., Koleva M., Ocvirk P., Le Borgne D., Soubiran C., 2007a, in Vazdekis A., Peletier R. F., eds, *IAU Symp. Vol. 241*, p. 68
- Prugniel P., Soubiran C., Koleva M., Le Borgne D., 2007b, preprint (arXiv:astro-ph/0703658)
- Prugniel P., Zeilinger W., Koleva M., de Rijcke S., 2011, *A&A*, 528, A128
- Rawle T. D., Smith R. J., Lucey J. R., 2010, *MNRAS*, 401, 852
- Salpeter E. E., 1955, *ApJ*, 121, 161
- S anchez Almeida J., Aguerri J. A. L., Mu oz-Tu n C., Vazdekis A., 2009, *ApJ*, 698, 1497
- S anchez-Bl azquez P., Gorgas J., Cardiel N., 2006a, *A&A*, 457, 823
- S anchez-Bl azquez P. et al., 2006b, *MNRAS*, 371, 703
- S anchez-Bl azquez P., Forbes D. A., Strader J., Brodie J., Proctor R., 2007, *MNRAS*, 377, 759
- Schroyen J., de Rijcke S., Valcke S., Cloet-Osselaer A., Dejonghe H., 2011, *MNRAS*, 416, 601
- Schweizer F., 1980, *ApJ*, 237, 303
- Seth A. C. et al., 2010, *ApJ*, 714, 713
- Simien F., Prugniel P., 2002, *A&A*, 384, 371
- Spolaor M., Proctor R. N., Forbes D. A., Couch W. J., 2009, *ApJ*, 691, L138
- Spolaor M., Hau G. K. T., Forbes D. A., Couch W. J., 2010a, *MNRAS*, 408, 254
- Spolaor M., Kobayashi C., Forbes D. A., Couch W. J., Hau G. K. T., 2010b, *MNRAS*, 408, 272
- Stetson P. B., Hesser J. E., Smecker-Hane T. A., 1998, *PASP*, 110, 533
- Thomas D., Maraston C., Bender R., 2003, *MNRAS*, 339, 897 (TMB)
- Tolstoy E. et al., 2004, *ApJ*, 617, L119
- Tonry J. L., Dressler A., Blakeslee J. P., Ajhar E. A., Fletcher A. B., Luppino G. A., Metzger M. R., Moore C. B., 2001, *ApJ*, 546, 681
- Valcke S., de Rijcke S., Dejonghe H., 2008, *MNRAS*, 389, 1111
- van Zee L., 2002, in Grebel E. K., Brandner W., eds, *ASP Conf. Ser. Vol. 285, Modes of Star Formation and the Origin of Field Populations*. Astron. Soc. Pac., San Francisco, p. 333
- van Zee L., Skillman E. D., Salzer J. J., 1998, *AJ*, 116, 1186
- van Zee L., Skillman E. D., Haynes M. P., 2006, *ApJ*, 637, 269
- Vazdekis A., Kuntschner H., Davies R. L., Arimoto N., Nakamura O., Peletier R., 2001, *ApJ*, 551, L127 (VAKU)
- Vazdekis A., S anchez-Bl azquez P., Falc n-Barroso J., Cenarro A. J., Beasley M. A., Cardiel N., Gorgas J., Peletier R. F., 2010, *MNRAS*, 404, 1639
- Wagner S. J., Bender R., Moellenhoff C., 1988, *A&A*, 195, L5
- Walker M. G., Mateo M., Olszewski E. W., Pe arrubia J., Evans N. W., Gilmore G., 2010, *ApJ*, 710, 886
- Welch G. A., Sage L. J., Mitchell G. F., 1998, *ApJ*, 499, 209
- Wernli F., Emsellem E., Copin Y., 2002, *A&A*, 396, 73
- White S. D. M., 1980, *MNRAS*, 191, 1p
- Young L. M., Lo K. Y., 1997, *ApJ*, 476, 127

APPENDIX A: IMAGE ANALYSIS AND PHOTOMETRY

We analysed archival GMOS images of the 14 galaxies from Spolaor et al. (2009), six in the Fornax cluster (FCC 148, FCC 153, FCC 170, FCC 277, FCC 301 and FCC 335) and eight in the Virgo cluster (VCC 575, VCC 828, VCC 1025, VCC 1146, VCC 1178, VCC 1297, VCC 1475 and VCC 1630). The data are acquisition images, taken before the spectra. We applied a standard procedure for bias subtraction and flat-fielding. The sky background was fitted with a low order polynomial on the edge of the detector and subtracted.

For the photometric analysis, we used our own software. The code starts from the light peak and choose a number of isophotal levels equidistant in mag arcsec⁻². These isophotes are sampled along directions separated by 5 , and fitted with ellipses. The errors are computed from the detector characteristics and background noise. Fitting the surface brightness variation along a given elliptical isophote with a fourth-order Fourier series, four more parameters can be derived that quantify how the isophotes deviate from pure ellipses. For instance, the fourth-order cosine term quantifies the boxiness/disciness of the isophotes. Except for two-component systems, such as the S0 galaxy FCC 153 which consists of a bulge and a very extended thin disc, such a model gives an excellent reproduction of the original image. The code has been tested by comparing its results with those derived from MIDAS and has proved its reliability. The techniques we use have been employed before (e.g. in De Rijcke et al. 2003a, 2006).

The total luminosity and effective radius were measured on the reconstructed image, and the S ersic parameters were fitted on the equivalent axis (i.e. geometric mean of the major and minor axes). The error bars were estimated using bootstrapping. Comparing the total luminosities measured from these models with the available HyperLeda values, we derived a mean *B*-band zero-point of $m_0 = 27.252$ mag arcsec⁻²/ADU which was applied to all data. With this value, we found very good agreement with the literature values. The parameters derived from this analysis can be found in Table 1.

APPENDIX B: SPECTRA FITS OF THE 1 ARCSEC EXTRACTIONS

In this section, we present the fits of the core extractions for the 40 galaxies in our sample, in order to illustrate the quality of the fits and visualize the misfits.

In the centre of all the Virgo galaxies of our sample, except in VCC 575 and 828, we observe a significant overabundance of Mg, and the Mg_b feature, near 5175  , is masked by the automatic kappa-sigma clipping (CLEAN option of the ULYSS command). As shown in Koleva et al. (2008a), this has no effect of the derived [Fe/H].

For the galaxies for which we fitted separately two observations (see Section 2.2) we present only one fit, as the two are almost identical. All the figures from this section are available electronically (see Supporting Information).

APPENDIX C: SAMPLE DESCRIPTION**C1 NGC 1375 = FCC 148**

This flat S0 galaxy ($\epsilon \sim 0.56$) has discy isophotes, strong rotation ($V_{\max} \sim 80 \text{ km s}^{-1}$) and $V_{\max}/\sigma > 1$. On the ACS images a clear peanut bulge is seen. A weak nebular emission is detected in the core. In the central 7 arcsec ($a_{\text{eff}} \sim 17 \text{ arcsec}$) the stellar population changes significantly. The metallicity decreases from 0.2 to -0.2 dex and the age rises from 1 to 2.5 Gyr. The σ -drop observed on the GMOS profiles is an artefact due to the wide slit.

The bulge clearly experienced a recent burst of star formation (100 to 300 Myr ago) fed by high metallicity gas.

C2 IC 335 = FCC 153

This galaxy has a prominent edge-on disc, and the isophotes cannot be fitted with ellipses (thus, the definition and value of a_{eff} can be debated). The photometric profile reveals the distinct bulge and disc components. The maximum rotation, V_{\max} , reaches 130 km s^{-1} , and $V_{\max}/\sigma > 1$. In the central region, out to 1–2 arcsec, the GMOS profile shows an important σ -drop, which is less marked on the FORS2 profile. Due to a lower S/N the FORS2 data were binned in the central region, but to check the hypothesis of a σ -drop we analysed the non-binned data: the 2 arcsec inner profile is consistent with a flat σ . So, we conclude that the GMOS drop is an artefact due to the wide slit (the effective spectral resolution is higher in the core). From the centre to a radius of 2 arcsec, the SSP-equivalent age rises from 3 to 5 Gyr and the metallicity drops from 0.25 to 0.05 dex. The flat σ profile may hide a central cold component that may be a young stellar disc.

The metallicity rises between 2 and 12 arcsec and decreases at larger distance. The position of this upturn corresponds to a minimum age and change of slope of the velocity dispersion profiles. At the peak, the metallicity reach super-solar values ($[\text{Fe}/\text{H}] = 0.2$ dex). The upturn corresponds also to the point where the disc stars to dominate the light. This complex profile likely reflects the combination between a bulge and a more metal-rich disc with a negative $\nabla_{[\text{Fe}/\text{H}]}$. Except in the centre, where young stars are present, the system has an intermediate age of around 5 Gyr.

C3 NGC 1381 = FCC 170

This is an S0 galaxy with a prominent edge-on disc in fast rotation ($V_{\max} \approx 170 \text{ km s}^{-1}$). The isophotes are not elliptical and the use of a_{eff} as a spatial scale may be questioned. The kinematical GMOS profiles display a σ -drop and a displacement of the kinematical centre in the central 2 arcsec. As this is not seen in the FORS2 profiles, this is an obvious artefact due to the wide slit.

The metallicity decreases from $[\text{Fe}/\text{H}] \sim 0.05$ to -0.15 dex within 3.5 arcsec. It remains constant out to $2 a_{\text{eff}}$, and then decreases to -0.7 dex at 60 arcsec. The centre of FCC 170 is older (12 Gyr) than the outskirts (7.5 Gyr). This is probably consistent with the decomposition into an old bulge and a younger disc.

C4 NGC 1428 = FCC 277

The isophotes of this galaxy are boxy and the flattening is $\epsilon \sim 0.5$. A foreground star, located 1 arcsec in the NE direction from the centre, was removed before performing the photometry. The galaxy rotates with $V_{\max} = 90 \text{ km s}^{-1}$, and $V_{\max}/\sigma > 1$. We classify it as E-S0 and assign it to the E group, though (Merluzzi et al. 1998)

classified is as S0. This galaxy was not observed with FORS2, and the σ -drop seen in the central 3 arcsec may be an artefact due to the wide slit used for this GMOS observing run (such an effect is observed in the other galaxies for which a comparison with narrow-slit observations is available). We extracted the stellar population parameters and kinematics out to $2 a_{\text{eff}}$. The metallicity drops from 0 to -0.7 dex in $1 a_{\text{eff}}$, while at $2 a_{\text{eff}}$ it is -1.3 dex. The age rises from 5 (centre) through 10 ($1 a_{\text{eff}}$) to 14 Gyr at $2 a_{\text{eff}}$.

C5 FCC 301

The isophotes of FCC 301 are slightly discy. We classify it as E-S0 and we assign it S0 group. Its ellipticity (ϵ) changes from 0.1 to 0.5 at 16 arcsec and then again descends to 0.14 at 150 arcsec. Out to 4 arcsec the velocity rises to 50 km s^{-1} , as a solid body and decreases outwards to a plateau of 20 km s^{-1} reached at a radius of 10 arcsec ($\sim 1 a_{\text{eff}}$). The velocity dispersion is constant within the solid-body region ($\sigma = 40 \text{ km s}^{-1}$) and it increases by 10–20 per cent outwards. The stellar population is homogeneous in the solid body region (5 Gyr and $[\text{Fe}/\text{H}] \approx -0.2$ dex), and the metallicity decreases and the age increases outwards.

C6 FCC 335

It is the only diffuse/dwarf elliptical galaxy in the sample of Spolaor et al. Its prominent nucleus is not resolved in our spectroscopic observations (we measure FWHM ~ 0.5 arcsec). The central isophotes are irregular, which is caused by the presence of dust, clearly seen on the composite image.⁷

We could fit the spectra a little bit further than $1 a_{\text{eff}}$, where the rotation velocity is $V = 30 \text{ km s}^{-1}$. The central velocity dispersion, $\sigma = 25 \text{ km s}^{-1}$, rises to 30 km s^{-1} at 6 arcsec (on the FORS2 profile; the kinematics on the GMOS profile are less precise due to the lower resolution). Such σ -drops are frequent in the dE galaxies; we note that it extends at a significantly larger scale than the nucleus. As other nucleated dwarfs (see further), it is suspected to possess lower metallicity in its centre.

C7 NGC 4318 = VCC 575

It is an elliptical (E3) galaxy with discy isophotes, a Sérsic index typical of low-luminosity galaxies (1.66) and a moderate flattening ($\epsilon_{\text{max}} = 0.33$ at $r = 65$ arcsec). The rotation velocity increases to $V_{\max} = 85 \text{ km s}^{-1}$ and reaches at 8 arcsec ($\sim 1 a_{\text{eff}}$). Then, it remains constant or decreases slightly. Over the same radial range where V rises, the velocity dispersion decreases from $\sigma_0 = 82 \text{ km s}^{-1}$ to $\sigma_{a_{\text{eff}}} = 55 \text{ km s}^{-1}$, and remains constant outwards. The age mildly rises from 6 to 8 Gyr, while the metallicity decreases outwards from a solar centre.

C8 NGC 4387 = VCC 828

This E4 galaxy has boxy isophotes. It has dynamically colder centre. The velocity dispersion rises from $\sigma_0 = 82 \text{ km s}^{-1}$ to $\sigma = 105 \text{ km s}^{-1}$ at 2 arcsec, further out it decreases to 75 km s^{-1} . The rotation velocity reaches $V_{\max} = 47 \text{ km s}^{-1}$ at $r = 15\text{--}20$ arcsec (i.e. $1 a_{\text{eff}}$). The profiles derived from the GMOS and VAKU observations are consistent.

⁷The ACS Fornax Cluster Survey, <https://www.cfa.harvard.edu/ajordan/ACSFCS/Gallery.html>

While the age is roughly constant (10 Gyr) along the body of the galaxy (out to the limit of the data at almost $2 a_{\text{eff}}$), the metallicity steeply decreases from super-solar to $[\text{Fe}/\text{H}] = -0.43$ dex at $1 a_{\text{eff}}$.

C9 NGC 4434 = VCC 1025

This E0 ($\epsilon = 0.04$) has perfectly elliptical isophotes. The rotation velocity reaches $V_{\text{max}} = 45 \text{ km s}^{-1}$ at 10–15 arcsec ($\sim 1 a_{\text{eff}}$) and remains constant afterwards. In the region with a velocity gradient, the velocity dispersion decreases from $\sigma_0 = 135 \text{ km s}^{-1}$ to $\sigma = 70 \text{ km s}^{-1}$. The age is uniformly old at about 10 Gyr, and the metallicity decreases monotonically with the radius. The slope of the metallicity profile changes at $r = 4$ arcsec, being steeper in the inner part of the galaxy.

C10 NGC 4458 = VCC 1146

This slowly rotating E0 galaxy ($\epsilon = 0.07$) harbours a kinematically decoupled core. In the inner 1.5 arcsec, the rotation reaches $V_{\text{max}} = 45 \text{ km s}^{-1}$ at 0.7 arcsec and vanishes at about 4 arcsec. Over this radial range, the velocity dispersion decreases from 130 to 85 km s^{-1} , and it slowly continues to decline at larger radius. Its kinetically decoupled core (KDC) was first noted by Halliday et al. (2001).

The stellar population parameters do not reflect the presence of a KDC. The population is old and the metallicity decreases monotonically. Morelli et al. (2004) study (with *Hubble Space Telescope* (*HST*) imaging and ground-based spectroscopy) these objects because of the presence of a nuclear stellar disc. They found that the nuclear disc is inclined at about 83° and has $L = 4.8 \times 10^6 L_{\odot, V}$. They did not find any significant gradient in the stellar population, but their data are restricted to the central region (up to $1/3 r_{\text{eff}}$). Their central metallicity is consistent with ours ($[\text{Fe}/\text{H}]_0 \sim -0.2$ dex).

C11 NGC 4464 = VCC 1178

It is an E2 galaxy ($\epsilon = 0.25$) with a Sérsic index $n = 2.31$ and discy isophotes. The central region rotates fast, reaching $V_{\text{max}} = 80 \text{ km s}^{-1}$ at 1.5 arcsec, while in the outskirts the rotation slowly decreases to 40 km s^{-1} . The central velocity dispersion is $\sigma_0 = 165 \text{ km s}^{-1}$ and it slowly decreases to 70 km s^{-1} . The age profile of the galaxy is flat (around 10 Gyr) and its metallicity slowly decreases from -0.2 to -0.4 dex at $1 a_{\text{eff}}$ (7.5 arcsec).

C12 NGC 4486B = VCC 1297

This is the only compact elliptical galaxy (cE) of our sample. This class of galaxies is characterized by a high mean surface brightness; we associate it to the E group. It has discy isophotes, harbours a double nucleus separated by 0.15 arcsec (Lauer et al. 1996) and hosts a super-massive black hole (Kormendy et al. 1997). This black hole is at the origin of the steep rise of the velocity dispersion in the centre: our central value reaches $\sigma_0 = 230 \text{ km s}^{-1}$, while Kormendy et al. (1997) measure $281 \pm 11 \text{ km s}^{-1}$ under better seeing conditions. The averaged velocity dispersion within an aperture of 2 arcsec is about 150 km s^{-1} ; with such a value, the galaxy would fall on the Fundamental Plane. While for the mean body of the galaxy the rotation velocity is constant ($V = 30 \text{ km s}^{-1}$), it peaks to $V_{\text{max}} = 60 \text{ km s}^{-1}$ at $r = 0.8$ arcsec (Kormendy et al. 1997) measure $76 \pm 7 \text{ km s}^{-1}$ at $r = 0.6$ arcsec).

The age has a mild negative gradient outwards, which is untypical for the rest of the E galaxies, but this characteristic is shared by at least one more cE (NGC 5846cE; Chilingarian & Bergond 2010).

The metallicity decreases from -0.15 dex in the centre to -0.6 dex at $4 a_{\text{eff}}$. This steep metallicity gradient was noticed first by Davidge (1991). The centre has an important overabundance in α -elements.

C13 NGC 4515 = VCC 1475

We classify this galaxy as E-S0 ($\epsilon = 0.2$), based on the images and on the slightly discy inner parts. The core, within 1 arcsec, is counter-rotating by about 2 km s^{-1} , with respect the bulk of the galaxy peaking at $V_{\text{max}} = 16 \text{ km s}^{-1}$ at $r = 5.5$ arcsec. The presence of the KDC is not reflected in the stellar population. The metallicity steeply decreases from $[\text{Fe}/\text{H}]_0 = -0.15$ dex to about -0.7 dex at $1 a_{\text{eff}}$.

C14 NGC 4551 = VCC1630

This is an E2 galaxy ($\epsilon = 0.26$) with a σ -drop in the centre. The velocity dispersion increases from $\sigma_0 = 90 \text{ km s}^{-1}$ to 100 km s^{-1} at $r = 2$ arcsec. The rotation velocity concomitantly reaches 30 km s^{-1} to continue to rise slowly to 40 km s^{-1} . The velocity dispersion declines to 80 km s^{-1} at $1 a_{\text{eff}}$.

The SSP-equivalent age of the core is about 2 Gyr younger than the bulk, aged about 9 Gyr. The metallicity decreases steeply from $[\text{Fe}/\text{H}]_0 = 0.17$ dex to -0.15 dex at 5 arcsec. It continues to decline slowly outwards.

Since the following galaxies were already described in De Rijcke et al., we will only recall some of their important characteristics.

C15 FCC 046

This is a dS0(dE4) galaxy. It is nucleated and detected in H α and H α . This TTD galaxy (according to our classification) is suspected in a central metallicity drop (Koleva et al. 2009a).

C16 FCC 136

This is a dE2 galaxy. We detected central depression in the metallicity profile (Koleva et al. 2009a, table 10).

C17 FCC 204

A dS0(6) galaxy, with spiral arms, visible after subtracting an axis-symmetric model. The fit to the photometric profile shows positive C_4 , an indication of the disciness. In the terminology of Lisker et al. (2007) it will be classified as dE(di).

C18 FCC 207

A dE2, nucleated galaxy suspected to have a central metallicity drop (fig. 2 of Koleva et al. 2009a). H α , H β , O III emission is detected.

C19 FCC 245

This is a nucleated galaxy (dE0). As for FCC 136 we detected a central depression of the metallicity (Koleva et al. 2009a, table 10). We find a ring of intermediate population, which is not seen in the images.

C20 FCC 266

This is a nucleated galaxy with a central depression in the metallicity profile (Koleva et al. 2009a, table 10).

C21 FCC 288

This is a dS0(7) galaxy with spiral underlying structure and a positive C_4 . As for FCC 204, it would be called dE(di) in the terminology of Lisker et al. (2007). We detected a central depression of the metallicity profile (Koleva et al. 2009a, table 10). It has a slight Mg_b underabundance.

C22 FS 76 = PGC 83852

This almost round dwarf has a kinematically decoupled core. Its velocity dispersion, which initially rises with the radius, starts to decline sharply outside of one half-light radius. Its Sérsic index of 2 indicates higher level of compactness than the other dEs at similar luminosity ($M_B = -17.1$ mag). This was interpreted as evidence for a truncated dark halo and, hence, for the occurrence of tidal striping (De Rijcke et al. 2001). Its metallicity profile regularly decreases from 0.2 to -0.2 dex in the central 3 arcsec. The presence of a KDC is not reflected by any particularity in the stellar population, thus the KDC should not be a recent event, but rather a long lived structure, which supports the tidal origin suggested in De Rijcke et al. (2004).

C23 FS 131 = PGC 83905

This is a dS0,N (dE5,N) dwarf. The central isophotes have a peanut shape.

C24 FS 373 = PGC 83270

This dE3 galaxy has a KDC. The ellipticity profile of the isophotes suggests the presence of a small central stellar disc (De Rijcke et al. 2004).

C25 NGC 5898 DW1 = PGC7 92714

This dE3 has a positive C_4 (De Rijcke et al. 2003a). Its flattening is stronger in the inner 10 arcsec ($\epsilon \sim 0.5$) than in the outskirts ($\epsilon \sim 0.2$). In the terminology of Lisker et al. (2007) it would be classified as a dE(di).

C26 NGC 5898 DW2 = PGC7 92560

DW2 is a nucleated dE6 with H α and H α emission. The metallicity profile is depressed in the centre (Koleva et al. 2009a, table10).

The next four SO galaxies are from the sample of Bedregal et al.

C27 FCC 055

It is a faint S0 with $M_B \approx -17.5$ mag and $\mu_B \approx 21.5$ mag arcsec $^{-2}$. However, it is more concentrated (Sérsic $n = 3$) than a typical dwarf galaxy. In the central part the isophotes are pointed (as expected from a disc presence), while in the outer parts they are elliptical. The $V_{\max} = 80$ km s $^{-1}$ is reached at 19 arcsec. While the ages and metallicities are mostly constant along the radius, there is a small depression at 2–3 arcsec associated with a rise in the velocity dispersion.

C28 NGC 1316 (Fornax A) = FCC 021

This peculiar galaxy, associated with the Fornax A radio source, has been interpreted since a long time as a merger remnant (Schweizer 1980), produced from a collision with a disc galaxy which occurred

1 to 3 Gyr ago (Bosma, Smith & Wellington 1985; Mackie & Fabbiano 1998). Despite these peculiarities, we associate it to the S0 group.

Our spectrum does not display significant nebular emission. Our measured velocity dispersion, $\sigma_0 = 239$ km s $^{-1}$, agrees with the values reported in HyperLeda. It is, however, significantly higher than the value found by Nowak et al. (2008) using IFU observations with adaptive optic at very high spatial resolution in the K band. These authors observe a central σ -drop, from 218 ± 8 km s $^{-1}$ at $r = 0.8$ arcsec to 226 ± 9 km s $^{-1}$ in an 8 arcsec aperture. It is possible that the optical and NIR observations do not trace the same kinematical population in this region affected by important dust extinction. The rotation velocity is monotonically rising to $V = 160$ km s $^{-1}$ at the limit of our data ($r = 45$ arcsec).

The SSP-equivalent age and metallicity are almost homogeneous at 4.7 Gyr and $[Fe/H] = 0.07$. The residuals from the fits do not indicate any strong α -elements enhancement. Our results differ from the ones of Kuntschner (2000), who finds an age of 2 Gyr and a very metal rich core with mild decrease of the metallicity along the radius.

C29 NGC 1380 = FCC 167

This is a fast rotating S0 galaxy ($V_{\max} \approx 210$ km s $^{-1}$), with a central velocity dispersion of 230 km s $^{-1}$. The age is constant along the radius. The metallicity first decreases by 0.2 dex (up to $1 a_{\text{eff}}$) and increases afterwards. We notice an Mg overabundance in the centre.

C30 NGC 1380A = FCC 177

This S0 shows the same metallicity behaviour as NGC 1380. We find $V_{\max} \approx 90$ km s $^{-1}$ and $\sigma_0 = 45$ km s $^{-1}$. The age is slightly younger (by 1 Gyr) in the centre than in the outskirts. We do not detect central strong Mg overabundance.

In the next paragraphs we describe the four remaining galaxies from VAKU, for which we do not have GMOS observations.

C31 NGC 4365 = VCC 0731

The image of this E3 galaxy reveals boxy, slightly hexagonal isophotes. This galaxy is known to have triaxial intrinsic shapes and kinematically decoupled core (Wagner, Bender & Moellenhoff 1988). Earlier stellar population studies (see Davies et al. 2001, and references therein) have shown a kinematical distinct inner region, which hosts the same stellar population as the outskirts. The galaxy harbours a metallicity gradient and constant age along the radius. Our profiles agree with the previous kinematical and stellar population studies (e.g. Davies et al. 2001).

C32 NGC 4473 = VCC 1231

This is an E5 galaxy with discy isophotes. Pinkney et al. (2003) argue that this galaxy underwent a recent merger because of its photometric peculiarities. They also find photometric and kinematic evidence for a cold stellar disc. Our analysis reveals a younger and more metal-rich core. The metallicity decreases outwards, changing its slope at 5 arcsec, where the maximum velocity (~ 60 km s $^{-1}$) is observed. The age is constant outside of this radius, but drops to about 6 Gyr inwards.

C33 NGC 4478 = VCC 1279

This E2 galaxy has a nuclear stellar disc (Morelli et al. 2004). We find that its central stellar population differs from the outskirts in sense that it is younger (5 Gyr old) and more metal rich.

C34 NGC 4621 = VCC 1903

This elliptical galaxy is known to host a counter-rotating core (Bender 1990; Wernli, Emsellem & Copin 2002); however its size is only 60 pc or 1 arcsec (Wernli et al. 2002) and it is barely visible in our data. However, we do observe a younger age and higher metallicity in the central pixel, in agreement with the central, blue colour observed by Krajnović & Jaffe (2004) using *HST*/WFPC2 data. It has an extended disc, seen from the isophote analyses (e.g. Bender 1990). Except for the central pixels, the age is constant along the radius; however its metallicity decreases steeply.

Finally, we will focus on the two nearby dwarf galaxies.

C35 NGC 205

A satellite of M31, NGC 205 is a prototype of massive dE, N. It has a dynamical mass of $4.5 M_{\odot}/L_{\odot}$ (De Rijcke et al. 2006) and a total magnitude $M_B = -16.0$. It has a maximum rotation velocity of $11 \pm 5 \text{ km s}^{-1}$ (Simien & Prugniel 2002; Geha et al. 2006) and its dispersion increases with the radius (Bender, Paquet & Nieto 1991; Simien & Prugniel 2002). It contains dust in the central 2 arcmin (Haas 1998), atomic and molecular gas (Welch, Sage & Mitchell 1998; Young & Lo 1997). Beyond the inner 1 arcmin radius it is dust and gas free and it has intermediate SSP-equivalent ages (Demers, Battinelli & Letarte 2003). There are evidence for a recent star formation (Baade 1944; Peletier 1993; Cappellari et al. 1999; Koleva 2009).

NGC 205 is suspected of close tidal interaction with M31 about 100 Myr ago (Cepa & Beckman 1988). We find that it has strong age/metallicity positive/negative gradients. The central age is 1 Gyr, while the central metallicity is -0.5 dex. At $1 r_{\text{eff}}$ the age rises to 10 Gyr, while the metallicity decreases to -1.3 dex.

C36 NGC 404

A nearly face-on dS0 galaxy, placed 3.4 Mpc (e.g. Tonry et al. 2001) from the Local Group and fairly isolated. It displays ongoing star formation (Ho, Filippenko & Sargent 1993) and a dust lane with complex structure within 5 arcsec from the centre (e.g. Gallagher 1986). del Río, Brinks & Cepa (2004) found a ring of neutral hydrogen (H I) ($M_{\text{H I}} = 1.5 \times 10^8 M_{\odot}$) surrounding the stellar disc. NGC 404 has also a low-ionization nuclear emission line region (LINER; Pogge et al. 2000).

Bouchard et al. (2010) performed spectroscopic studies and found a complex star formation history (with more recent star formation near the centre), nearly flat metallicity and age profiles within the inner 20 arcsec and decreasing/increasing ages/metallicities outside. Here, we used the same observations as in Bouchard et al. (2010). NGC 404 has a very peculiar kinematical structure with two inversions of the velocity gradient, and the innermost region ($r < 3$ arcsec or 45 pc) of the galaxy rotates in the same direction as the H I (del Río et al. 2004; Bouchard et al. 2010). This inner core is also the region where the youngest stars were found (Bouchard et al. 2010).

SUPPORTING INFORMATION

Additional Supporting Information may be found in the online version of this article.

Figures B1– B10. Fits of the core extractions for the 40 galaxies in our sample.

Please note: Wiley-Blackwell are not responsible for the content or functionality of any supporting materials supplied by the authors. Any queries (other than missing material) should be directed to the corresponding author for the article.

This paper has been typeset from a $\text{\TeX}/\text{\LaTeX}$ file prepared by the author.